Holocene offshore tsunami archive – Tsunami deposits on the Algarve shelf (Portugal)

Lisa Feist [a],[*], Pedro J.M. Costa [b],[c], Piero Bellanova [a], Ivana Bosnic [b], Juan I. Santisteban [d], César Andrade [b], Helmut Brückner [e], João F. Duarte [f], Jannis Kuhlmann [g], Jan Schwarzbauer [h], Andreas Vött [i], Klaus Reicherter [a], the M152 shipboard scientific party [1]

[a] Institute of Neotectonics and Natural Hazards, RWTH Aachen University, Germany
[b] Instituto D. Luiz, Faculdade de Ciências, Universidade de Lisboa, Portugal
[c] Department of Earth Sciences, Faculty of Sciences and Technologies, University of Coimbra, Portugal
[d] Department of Geodynamics, Stratigraphy and Paleontology, Fac. Geological Sciences, Universidad Complutense de Madrid, Spain
[e] Institute of Geography, Department of Geosciences, University of Cologne, Germany
[f] Divisão de Geologia Marinha, Instituto Hidrográfico, Portugal
[g] MARUM – Center for Marine Environmental Sciences, Research Faculty, University of Bremen, Germany
[h] Laboratory for Organic-Geochemical Analysis, Institute of Geology and Geochemistry of Petroleum and Coal, RWTH Aachen University, Germany
[i] Institute of Geography, Natural Hazard Research and Geoarchaeology Group, Johannes Gutenberg-Universität Mainz, Germany

ARTICLE INFO

ABSTRACT

The well-known 1755 CE Lisbon tsunami caused widespread destruction along the Iberian and northern Moroccan coastlines. Being affected by the powerful 1755 CE Lisbon tsunami, the southwestern Algarve shelf provides environments for detecting offshore tsunami imprints. Our multidisciplinary investigations (hydroacoustics, sedimentology, geochemistry, radiocarbon dating) of the Holocene sediments have revealed tsunami deposits linked to this tsunami and a ca. 3600 cal yr BP event. The latter event is until now unidentified in Portugal. Both event deposits contrast with the background shelf sedimentation by their coarser grain size, element composition, internal structure, and erosive base, making them discernible in the sub-bottom data and cores. Especially the ca. 3600 cal yr BP deposit is exceptionally well-preserved at one of the coring sites. The clear differentiation into several sections enables further insights into offshore tsunami transport and depositional processes. This study demonstrates that the record and preservation of tsunami deposits were possible on the Algarve shelf in specific locations sheltered from possible alterations. Our findings extend the tsunami catalogs of Portugal with a previously unknown tsunami dated to ca. 3600 cal yr BP.

1. Introduction

Sedimentary imprints of high-energy events on the continental shelves are commonly associated with high-density sediment flows triggered by floods, storms, submarine slope failures, or tsunamis (Einsele et al., 1996). These events are recorded as erosive or depositional features on the continental shelves; and as secondary mass movements and turbidites beyond the shelf break (Einsele et al., 1996; Dawson and Stewart, 2007). Floods, storms, and tsunamis can severely affect coastal societies, local economies, and environments. The research on sedimentological imprints of these events has relied on onshore studies where impacts are more evident compared to the offshore domain. However, the Holocene record of these events can be more complete in offshore areas where the deposits are protected from common onshore post-depositional alterations (e.g., changes in coastal morphology, erosion, weathering, pedogenesis, anthropogenic modification) (Szczuciński, 2012, 2020; Spiske et al., 2020). On the other hand, offshore sedimentary signatures are highly variable and can be altered through sediment erosion, mixing, deposition, or bioturbation (Wheatcroft and Drake, 2003; Wheatcroft et al., 2007). Therefore, the preservation of sedimentary signatures is especially favored in depositional sinks (i.e., small basins) below the storm wave base, where sediment is sheltered from currents and waves.

Storms are powerful geomorphic agents primarily acting as key erosional players removing sediment towards the nearshore and, resulting from backflow, towards offshore areas (Brenchley, 1989; Einsele et al., 1996). On the other hand, tsunami waves exceed storm waves in terms of wavelength and water mass transport, and thus can provide significant depositional signatures further inland and, in the case of tsunami backflow, distinctive beds in shallow shelf waters (Einsele et al., 1996). Research on tsunami deposits underwent substantial progress during the last three decades. Nevertheless, little is still known about offshore tsunami deposits, particularly their related depositional mechanisms and diagnostic features. Thus, a substantial part of the tsunami depositional process lacks detailed understanding. Several studies focused on offshore tsunami impact following significant events, e.g., 2011 Tōhoku-Oki (Arai et al., 2013; Ikehara et al., 2014; Tamura et al., 2015); 2004 Indian Ocean (Feldens et al., 2009, 2012; Sakuna et al., 2012; Sakuna-Schwartz et al., 2015); 2009 South Pacific (Riou et al., 2020a, 2020b). Paleo-tsunami deposits were also described in historic and prehistoric contexts, e.g., the 1883 CE Krakatoa eruption (van den Bergh et al., 2003); various events in the Mediterranean Sea (Smedile et al., 2011, 2020; Goodman-Tchernov and Austin, 2015; Goff et al., 2018); a before undocumented event in the Red Sea (Goodman Tchernov et al., 2016); and the 1755 CE Lisbon tsunami (Abrantes et al., 2008).

Like onshore tsunami deposits, offshore deposits can hardly be generalized regarding their sedimentological characteristics and geophysical and geochemical properties. Different characteristics are attributed to different hydrodynamic conditions during the inundation and backwash phases (Sakuna et al., 2012) and site-specific factors (e.g., bathymetry, channeling effect, sediment supply, preservation potential, and bioturbation). Nevertheless, many offshore tsunami deposits are characterized by erosional basal surfaces (Feldens et al., 2012; Sakuna et al., 2012; Ikehara et al., 2014; Smedile et al., 2020). Sedimentary features found in offshore tsunami deposits include reworked marine sediments and increased terrigenous materials (Feldens et al., 2012; Tamura et al., 2015; Riou et al., 2020a, 2020b; Smedile et al., 2020). Terrigenous materials are eroded onshore and transported by the tsunami backwash channeled in submarine valleys as high-density flows (Dawson and Stewart, 2007; Abrantes et al., 2008; Feldens et al., 2009; Bahlburg and Spiske, 2012; Goodman Tchernov et al., 2016; Riou et al., 2020a, 2020b).

The littoral areas of the Algarve, southern Portugal, are densely populated and highly important for the Portuguese economy, especially for the tourism sector (Omira et al., 2011). Storms along the Algarve coast occur frequently and can lead to severe short-term alterations of the littoral (Harley et al., 2014). The well-known 1755 CE Lisbon tsunami devastated large areas of the Iberian and northern Moroccan coastlines (Baptista and Miranda, 2009). Baptista and Miranda (2009) list several other tsunami events in their catalog. Tsunamigenic earthquakes along the Iberian Atlantic coast are related to the compressive tectonic setting within the Eurasian-African plate boundary (Baptista et al., 1998) with a transcurrent motion of the Gloria Fault (Kaabouben et al., 2008) or the effect of distant seismic sources (i.e., the Azores or Grand Banks; Baptista and Miranda, 2009). Tsunamis are also possible as a consequence of mass wasting events in the Gulf of Cádiz (Mulder et al., 2009) or the volcanic Atlantic archipelagos (Krastel et al., 2001).

This study focuses on the Algarve continental shelf with areas close to Alcantarilha and Salgados for the eastern sector, and Martinhal and Boca do Rio for the western sector (Fig. 1). This part of the Portuguese coast was heavily affected by the 1755 CE Lisbon tsunami. While the southwestern Iberian onshore record related to this event is well-studied (Fig. 1B) (Costa et al., 2021 for a summary), little emphasis has been laid on the correlated offshore imprint and associated hydrodynamic processes. Along the study area of the Algarve shelf, only a few offshore tsunami studies were conducted by Costa et al. (2012a, 2012b) (Fig. 1B: e, f), who compared the onshore and nearshore 1755 CE Lisbon tsunami sediments and Quintela et al. (2016) (Fig. 1B: g, j) who compared foraminifera assemblages onshore and from a sediment core of the outer shelf. Mendes et al. (2020) (Fig. 1B: k) analyzed the Guadiana River paleo-

valley for flooding events but did not identify deposits related to the 1755 CE tsunami. In terms of paleo-tsunamis, the Algarve onshore record is complex, particularly before ca. 3000 cal yr BP, before the full development of coastal barriers (Andrade et al., 2004, 2016; Costa et al., 2016).

This study investigates the Holocene sedimentary record of the Algarve continental shelf off southern Portugal to identify offshore deposits of the 1755 CE Lisbon tsunami and possible preceding events and assess their sedimentological features. To do so, RV METEOR cruise M152 (Reicherter et al., 2019) recorded hydroacoustic profiles and collected sediment cores from the shelf. We present hydroacoustic profiles and sediment cores from two different transects on the Algarve shelf (Fig. 1C) containing several intercalated event deposits. These deposits were analyzed using a multi-proxy approach that combined sedimentological methods (high-resolution grain size analyses), P-wave velocity, magnetic susceptibility, and XRF core-scanning. The chronological framework was established by radiocarbon dating.

2. Area descriptions

The Algarve continental shelf, with a mean width of approximately 17 km, dips gently until the shelf break at 110–150 m water depth (Fig. 1C). It experienced significant environmental changes since the Last Glacial Maximum (ca. 20,000 cal yr BP) when sea level was approximately 120–130 m lower than today (Dias et al., 2000; Lambeck et al., 2014). During the rapid post-glacial sea level rise, the coastline retreated landwards until ca. 5000–6000 cal yr BP, changing the width and the water depth distribution over the shelf (Dias et al., 2000).

The Algarve shelf is characterized by some bathymetric features, such as the Portimão canyon and rocky pinnacles consisting of resistant rocks of Mesozoic and Cenozoic ages (see Geological Map, Appendix B). The dominant swell direction is from (south)west, i.e., from the North Atlantic. The western study area is partly sheltered from these waves by the S. Vicente cape (Costa and Rita, 1992; Costa et al., 2011). Storms are frequent along the coast (Harley et al., 2014) even though only a few corresponding onshore storm deposits are documented (Andrade et al., 2004; Kortekaas and Dawson, 2007) (Fig. 1B: a, h). Storm waves from west to southwest reach about 3–4 m significant wave height with a mean period of 7–8 s on average once every winter (Costa and Rita, 1992). Strong easterly winds (*Levante*) produce slightly lower significant wave heights in the study area (Costa and Rita, 1992). Sedimentary shelf archives below the storm wave base and untouched by ocean currents, such as the Mediterranean Outflow Water (MOW), are suitable for paleo-tsunami research based on the high preservation potential. For the western Algarve, the MOW, a complex system of currents that flow westward from the Mediterranean Sea through the Strait of Gibraltar into the Gulf of Cádiz, is at depths of 400–600 m (Mediterranean Upper Water) and 600–1500 m (Mediterranean Lower Water) (Baringer and Price, 1997, 1999). The sedimentary archives analyzed in this study (Table 1; 65–113 m water depths) are located above the influence of the MOW and below the mean level of the storm wave base at around 30–35 m water depths (Hernández-Molina et al., 2000).

3. Methods and material studied

Multibeam surveys were conducted using two hull-mounted Kongsberg echosounder systems, EM122 (12 kHz) and EM710 (70–100 kHz), permanently installed on RV METEOR. Water depth levels for parasound profiles were taken from the EM122. The Atlas Parasound P70 system installed onboard RV METEOR can emit two primary high frequencies of 18 kHz and 18.5–28 kHz, thus generating parametric secondary low frequency between 0.5 and 6 kHz used for the sub-bottom survey. A vertical resolution of <15 cm in sediment and maximum penetration of 30 m below the seafloor surface was obtained. Aquaculture installations occupying the near-coastal zone prevented navigation further coastwards to reach even shallower shelf areas.
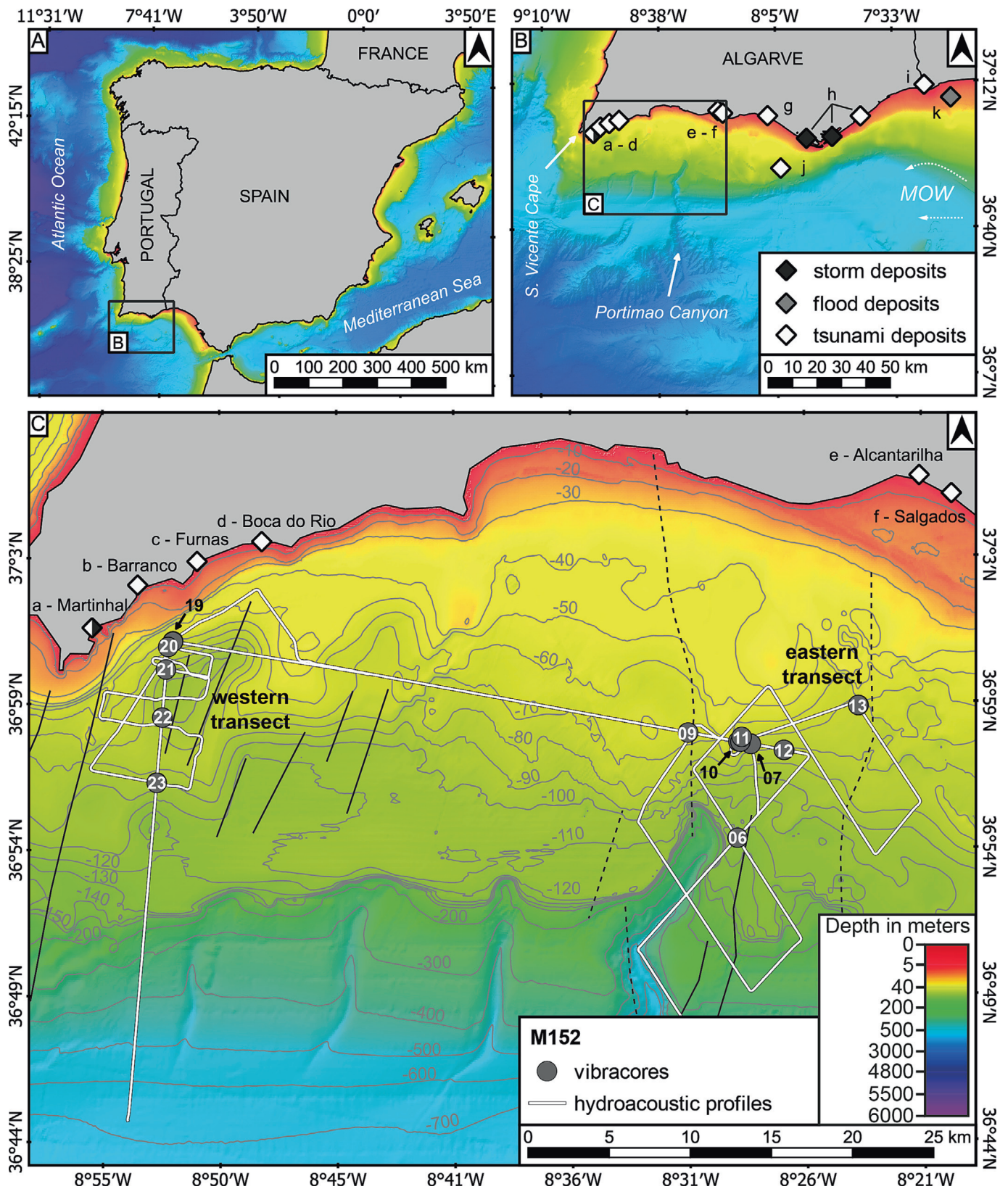
Fig. 1. A: Location of the study area in western Europe. B: Overview of the Algarve and locations of known tsunami and flood deposits from the literature (based on Costa et al., 2021 if not indicated otherwise): a) Martinhal, b) Barranco, c) Furnas, d) Boca do Rio, e) Alcantarilha, f) Salgados, g) Quarteira, h) Ria Formosa, i) Guadiana, j) offshore Quarteira (Quintela et al., 2016), k) offshore Guadiana (Mendes et al., 2020). In addition, the S. Vicente Cape and Portimão Canyon are marked on the map, as well as the general direction of the MOW (=Mediterranean Outflow Water). C: Overview of the southwestern Algarve shelf with hydroacoustic profiles and vibracores of this study. Solid black lines indicate the locations of faults on the shelf, and dashed black lines indicate the presumed locations of faults on the shelf as indicated in the Geological Map of the area (see Appendix B). All coring locations were labeled GeoB235 (core repository identifier) followed by the station number (e.g., GeoB23523), but for better readability, the prefix GeoB235 is not included here and in the text. The EMODnet Bathymetry DTM was used to show the mean depth in rainbow colors in all maps (EMODnet Bathymetry Consortium, 2020).

Table 1

Sample location, recovery, and water depth of the retrieved vibracores from the western and eastern transects during RV METEOR cruise M152. See the cruise report (Reicherter et al., 2019) for further information. Analyses: GS = grain-size determination, PW = P-wave velocities, MS = magnetic susceptibility, XRF = X-ray fluorescence, 14C = radiocarbon dating.

Cores GeoB235…	Latitude [°N]	Longitude [°W]	Water depth [m]	Recovery [m]	Transect	Analyses
06-01	36° 54.853	008° 27.957	111	0.75	East	GS
07-03	36° 57.173	008° 28.275	79	4.86	East	PW, MS, XRF
09-01	36° 57.563	008° 30.876	66	2.64	East	GS, PW, MS, XRF, 14C
10-01	36° 57.260	008° 28.792	69	3.62	East	GS, PW, MS, XRF
10-02	36° 57.250	008° 28.709	70	2.40	East	GS, XRF, 14C
11-01	36° 57.408	008° 28.655	73	4.06	East	PW, MS, XRF
12-01	36° 56.963	008° 26.893	93	4.37	East	PW, MS, 14C
12-02	36° 56.968	008° 26.906	92	4.34	East	PW, MS, XRF
13-01	36° 58.447	008° 23.792	70	4.76	East	PW, MS, XRF
13-01	36° 58.447	008° 23.808	69	5.27	East	PW, MS
19-01	37° 00.656	008° 52.247	65	3.56	West	GS, PW, MS, XRF, 14C
19-02	37° 00.654	008° 52.260	65	3.65	West	GS, MS, XRF, 14C
19-03	37° 00.643	008° 52.258	66	3.60	West	GS, MS, XRF
20-01	37° 00.469	008° 52.455	69	3.61	West	GS, PW, MS, XRF
21-01	36° 59.717	008° 52.549	74	3.14	West	GS, PW, MS, XRF
22-01	36° 58.120	008° 52.703	88	4.21	West	GS, PW, MS, XRF, 14C
22-02	36° 58.114	008° 52.705	88	4.63	West	MS, XRF
23-01	36° 55.951	008° 52.938	113	3.23	West	GS, PW, MS, XRF

In 65–113 m water depth, 19 sediment cores were retrieved using a vibracoring system based on a ROSSFELDER P-5C and P-3C electric high-frequency vibro-percussive head, with a maximum sediment recovery of 5.48 m. Sampling sites were georeferenced using high-precision navigation equipment (CNAV-DGPS). P-wave velocity was measured along the closed cores at an interval of 2.5 cm with PUNDIT LAB equipment.

Subsequently, the sediment cores were cut into ca. 1 m long sections and opened in the laboratories on board RV METEOR or at RWTH Aachen University. All sections (opened and intact) were stored at a temperature of 4 °C. On the opened sections, litho-stratigraphic units were identified by visual sediment description. Volume-specific magnetic susceptibility was analyzed with a Bartington MS2K (resolution of 2 cm, accuracy of 1.0 SI). X-ray fluorescence scans (XRF) were measured using an ITRAX core scanner (resolution 2 mm, 20 s exposure time, 30 kV, 55 mA). The retrieved dataset of element counts has been cleared from or adjusted by interfering peaks, double peaks, elementary composition, and tube parameters. XRF data were treated using the ItraXelerate software (Weltje et al., 2015). Single-element relative concentrations have been transformed using a multivariate log-ratio calibration (MLC) following Weltje et al. (2015), and log-ratios following Weltje and Tjallingii (2008) have been used.

For textural analysis, the cores were sub-sampled (1 cm resolution for the first 1.8 m and 10 cm resolution for the rest of the cores). Bulk samples were sieved using a standard set of sieves at 0.5 Φ intervals (up to 1 Φ). Smaller grain sizes were measured with laser granulometry (Malvern Mastersizer Hydro 2600 MU). Statistical parameters were calculated and plotted in GRADISTAT (Blott and Pye, 2001). Sediment size terms were based on the Wentworth (1922) scale and qualitative classification of sediment sorting, skewness, and kurtosis, followed Folk and Ward (1957).

A total of 33 samples were 14C-dated at Beta Analytic Inc. (USA) and Keck Carbon Cycle AMS Facility (UC Irvine, USA). Calibration was done with CALIB 8.2 (Stuiver and Reimer, 1993; Stuiver et al., 2023) using Marine20 (Heaton et al., 2020) and IntCal20 (Reimer et al., 2020) calibration curves. Local age-specific reservoir effect values were recalculated and applied; further information can be found in Appendix C. The sample from core 10-02 at 0.24 mbsf was calibrated with CALIBomb (Reimer et al., 2004; Reimer and Reimer, 2023) using the NHZ2 (Hua et al., 2013) and IntCal20 (Reimer et al., 2020) datasets after subtracting the global and local reservoir effects. Age-depth models were created using OxCal version 4.4 (Bronk Ramsey, 2009) and the depositional model (Bronk Ramsey, 2008; Bronk Ramsey and Lee, 2013). See Appendix C for more information on laboratory facilities, the used local reservoir effects, and the calculated age-depth models.

4. Results and analyses

4.1. The hydroacoustic survey

The hydroacoustic survey included sub-bottom profiles to visualize the shallow sedimentary cover of the shelf and to facilitate the recognition of depositional sinks, basins, and submarine valleys as the most suitable coring locations. According to the profiles, the study area is generally marked by relatively rugged erosional seafloor and frequent exposures of bedrock. Sub-bottom profiles indicate different penetration depths varying from near 0 m in areas where bedrock is exposed (i.e., no sedimentary cover) to a maximum of around 30 m in areas with high accumulation rates. The sub-bottom profiles also indicate different environmental conditions between the eastern and western transects (Fig. 2).

All coring stations and cores were labeled GeoB235 (core repository identifier), followed by the station number. Duplicate and triplicate cores are differentiated with the station number followed by -01, -02, and -03 (e.g., GeoB23509-01). However, for better readability, the prefix GeoB235 is not included in the text and figures.
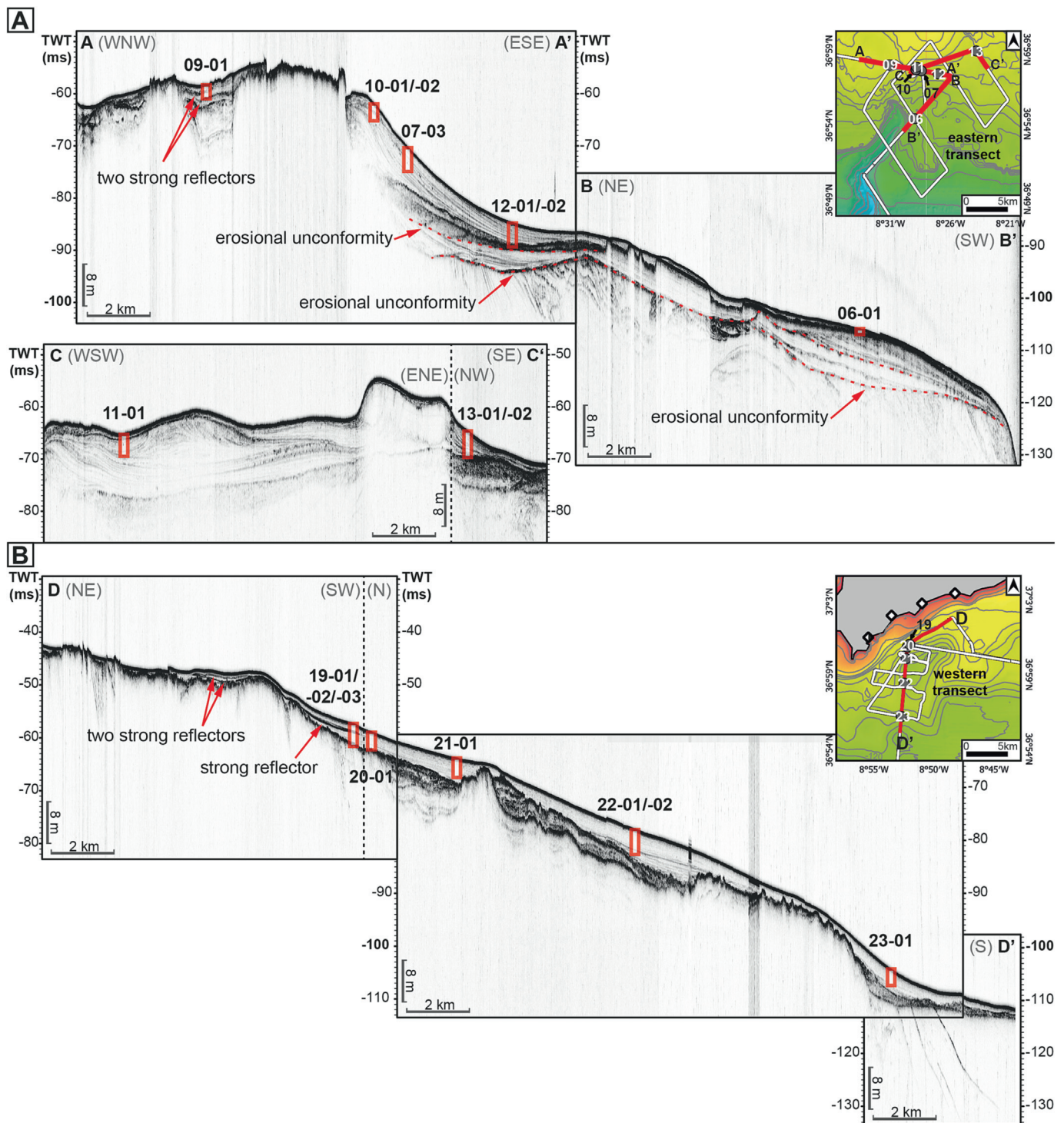
4.1.1. The eastern transect

The eastern transect (Fig. 2A) is characterized by a wide shelf with the Portimão canyon as a prominent feature. This transect mostly corresponds to a sediment-starved shelf expansion featuring numerous rocky outcrops. Sediment depocenters are confined to isolated basins (e.g., location of core 09-01 under 66 m water depth; Table 1), including fault-controlled depressions at the westernmost region of the transect and a sedimentary prism that thins towards the south and east, at the eastern end of the transect. This large sedimentary body was sampled by cores 06-01, 07-03, 10-01, 10-02, 11-01, 12-01, and 12-02 between 69 and 111 m water depths (Table 1). Cores 13-01 and 13-02 were sampled northeast of the sedimentary prism in 69 and 70 m water depth separated from that prism by a rock outcrop. Several erosional unconformities complicate the stratigraphic correlation among the cores. At core location 09-01, two particularly strong reflectors are found at around 1 mbsf (meters below seafloor) and 2.6 mbsf, which indicate coarse or compacted materials.

4.1.2. The western transect

The western transect (Fig. 2B) is located along a basin constrained by an NNE-SSW horst-graben fault system marked in the geological map of the area (Appendix B). The hydroacoustic profiles show an aggrading pattern with wide and thin sediment bodies, indicating low

Fig. 2. Sub-bottom profiles of the study area. A: Interpretation of the sub-bottom profiles of the eastern transect. B: Interpretation of the sub-bottom profiles of the western transect. TWT = Two-way travel time. Note that all profiles are vertically exaggerated.

sedimentation rates, i.e., a sediment-starved shelf. Coring sites 19-01, 19-02, 19-03, 20-01, and 21-01 (65–74 m water depths; Table 1) are located on an upper plateau confined by a steep NE-SW slope to the northwest that dips around 4° to the southeast. Cores 22-01, 22-02, and 23-01 (88 m and 113 m water depths, respectively; Table 1) are located on a gentle slope dipping towards a deeper area below 100 m water depth. Profiles from the shallower part of the shelf (<70 m water depth) reveal a distinctive strong reflector within the sedimentary cover (Fig. 2D). Near site 19, the strong reflecting layer has been

found around 1.25–1.60 mbsf (Fig. 2B). This strong reflector is restricted to the shallow area and is not visible in sites 20 and 21. This reflector splits into two in shallower waters <40 m water depth.

4.2. Results from coring

In total, 18 vibrocores were obtained from shelf sediments (Table 1), which were analyzed and radiocarbon dated. Like the sub-bottom profiles, the cores indicate different characteristics between the eastern

and western transects, with generally coarser sediments in the east and finer-grained sediments in the west. In broad terms, the cored stratigraphy is divided into a coarse unit at the base that fines upwards and transitions into a thick finer-grained unit until the top of the cores (Fig. 3). One or more laterally discontinuous coarser-grained layers were found intercalated in the upper finer-grained unit.
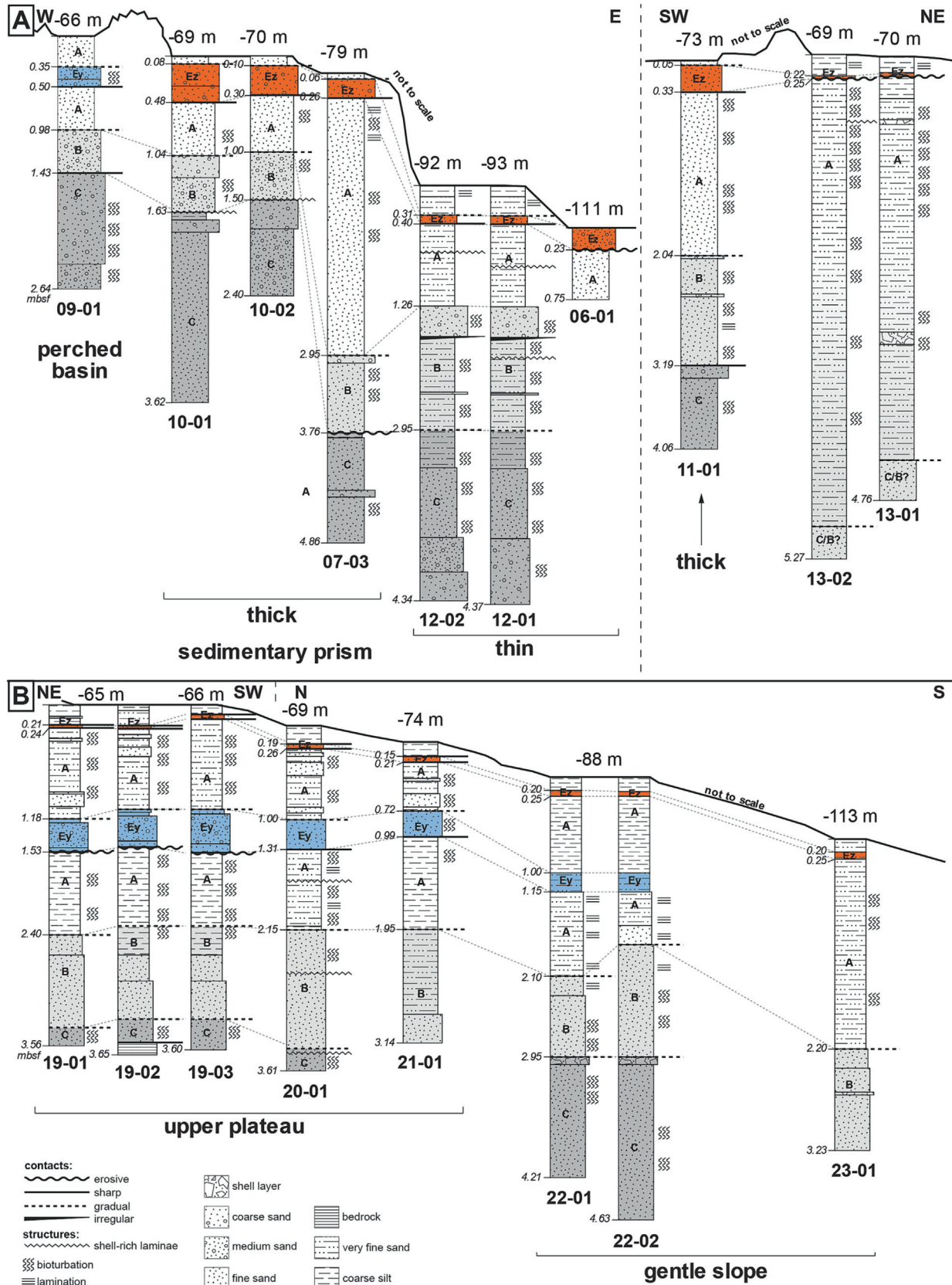

Fig. 3. Stratigraphic profiles of the eastern and western transects with water depths. A: Stratigraphic profiles of the eastern transect. B: Stratigraphic profiles of the western transect.

4.2.1. The cores of the eastern transect

Cores collected from the eastern transect can be separated into four groups based on their location, and sedimentary facies (Fig. 3A): group a) core 09-01, with two strong reflectors in the sub-bottom profiles was retrieved from a perched basin, group b) cores 07-03, 10-01, and 11-01 taken from the thicker part of the sediment prism referred above, group c) cores 06-01, 12-01, and 12-02 from the thinner part of that sediment prism, and group d) cores 13-01 and 13-02 separated from the sediment prism.

Core 09-01: core 09-01 recovered 2.64 m of sediment (Fig. 3A, Table 1).

- The top of the core between 0 and 0.35 mbsf is composed of homogenous poorly sorted fine sand (mean: 2.7 Φ, sorting: 2.5 Φ; Fig. 4). The grain size is distributed between 0.8–7.0 % gravel, 72.7–76.9 % sand, 16.1–23.8 % silt, and 1.5–2.6 % clay. The sediments are slightly fining upwards, and laminations occur. In addition, a well-preserved Pectinidae fragment was found.

- Between 0.35 and 0.50 mbsf, the grain size is coarser than in the surrounding sediments of unit C. The upper part (0.35–0.45 mbsf) is generally coarser-grained with very poorly sorted medium sand (mean: 2.0 Φ, sorting: 3.0 Φ; Fig. 4) and occasional bioclast fragments. The grain size is distributed between 9.5 % gravel, 66.1 % sand, 21.9 % silt, and 2.5 % clay. A thin mud lamina separates the upper and lower parts of this deposit (1.3 % gravel, 63.0 % sand, 32.1 % silt, and 3.6 % clay). The lower part of this deposit (0.45–0.50 mbsf) is composed of very poorly sorted fine sand (mean: 2.4 Φ, sorting: 2.8 Φ; Fig. 4) that contains large fragments of broken bioclasts, mainly bivalves, especially along the abrupt basal contact. The grain size is distributed between 5.8 % gravel, 77.7 % sand, 14.9 % silt, and 1.6 % clay.

- Between 0.50 and 0.98 mbsf, the core consists of homogenous poorly sorted fine sand (mean: 2.7 Φ, sorting: 2.5 Φ; Fig. 4), similar to the top. The grain size is distributed between 0.5–9.5 % gravel, 55.3–79.1 % sand, 16.9–39.1 % silt, and 1.6–5.1 % clay.

- Between 0.98 and 1.43 mbsf, the core comprises a very poorly sorted lithic and bioclastic medium sand deposit with an upwards-increasing fine-grained matrix content (mean: 1.1 Φ, sorting: 2.7 Φ; Fig. 4) resting over a sharp contact surface. A sudden decrease in coarse grains marks the upper contact of this unit. The grain size is distributed between 7.6–42.0 % gravel, 41.6–77.0 % sand, 6.6–19.8 % silt, and 1.1–2.0 % clay.

- Between 1.43 and 2.64 mbsf, the base of the core is composed of moderately sorted medium to coarse sand (mean: 1.2–0.2 Φ, sorting: 1.2–0.6 Φ; Fig. 4). The grain size is distributed between 0.0–21.1 % gravel, 77.6–100.0 % sand, 0.0–1.4 % silt, and 0.0–0.2 % clay. Bivalves and gastropods of different sizes occur, both broken and fully preserved.

Cores 07-03, 10-01, 10-02, 11-01: cores 07-03, 10-01, 10-02, and 11-01 show, in broad terms, identical stratigraphical arrangement, with the upper units of cores 10-01 and 10-02 being much more condensed compared to cores 07-03 and 11-01 (Fig. 3A). The total sediment recovery amounts to 4.86 m, 3.70 m, 2.40 m, and 4.08 m for cores 07-03, 10-01, 10-02 and 11-01, respectively (Table 1).

- Between 0 and 0.06 mbsf in core 07-03, 0 and 0.08 mbsf in core 10-01, 0 and 0.10 mbsf in core 10-02, and 0 and 0.05 mbsf in core 11-01, the top part of all cores are composed of homogenous very poorly sorted medium to fine sand that is slightly fining upwards (mean: 1.7 Φ, sorting: 1.0 Φ), and contain more shell fragments towards the top. The grain size is distributed between 4.9–10.9 % gravel, 72.5–82.6 % sand, 10.8–14.7 % silt, and 1.7–1.9 % clay.

- Between 0.06 and 0.26 mbsf in core 07-03, 0.08 and 0.48 mbsf in core 10-01, 0.10 and 0.30 mbsf in core 10-02, and 0.05 and 0.33 mbsf in core 11-01, a coarser-grained deposit differs from the surrounding sediments. This deposit comprises very poorly sorted bioclastic coarse sand (mean: 1.1 Φ, sorting: 1.2 Φ) with coarse shell fragments. In core 10-01, this deposit can be separated into an upper and a lower section. The upper section is composed of generally finer grains (4.6 % gravel, 67.8 % sand, 24.4 % silt, and 3.2 % clay), while the lower section consists of coarse grains and shell fragments above an erosive base (5.7–9.9 % gravel, 73.2–78.6 % sand, 13.1–18.6 % silt, and 1.8–2.6 % clay).

- Between 0.26 and 2.95 mbsf in core 07-03, 0.48 and 1.04 mbsf in core 10-01, 0.30 and 1.00 mbsf in core 10-02, and 0.3 and 0.2.04 mbsf in
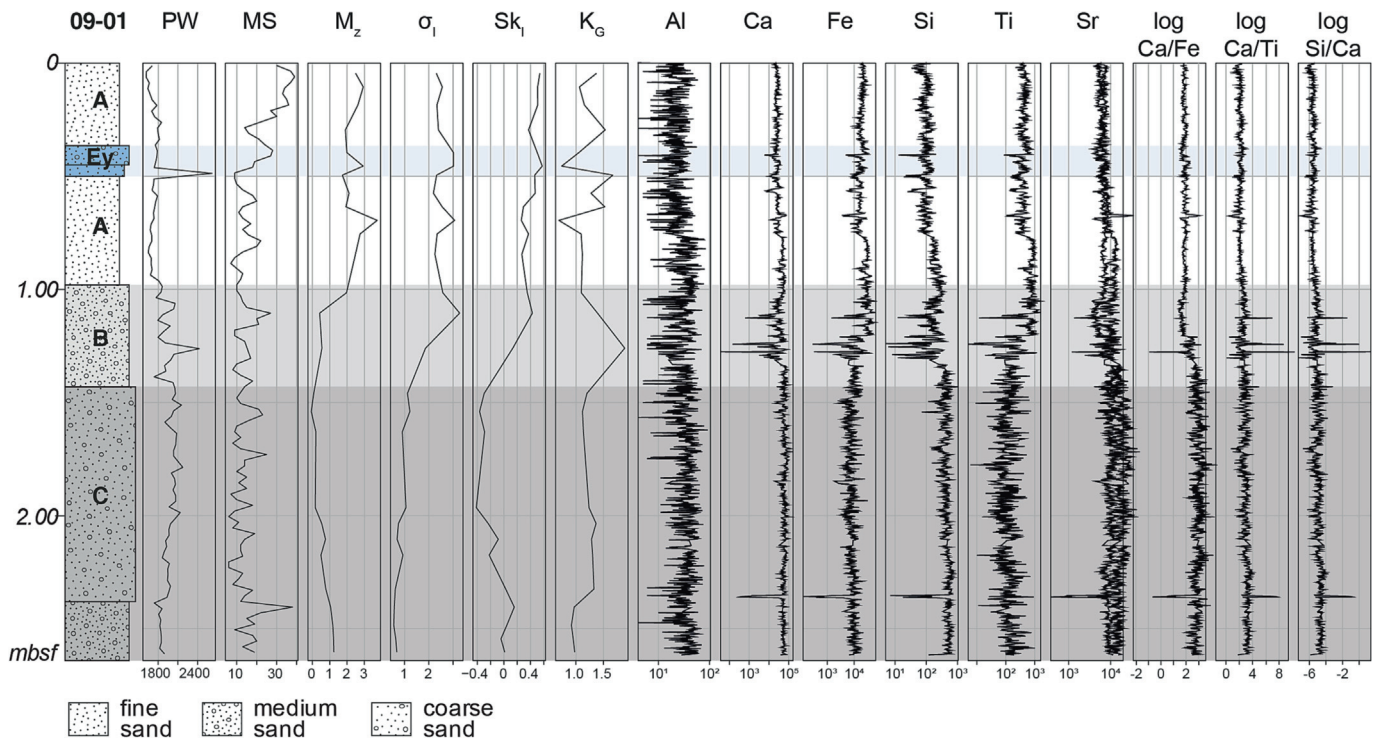

Fig. 4. Structural, textural, compositional properties of core 09-01 (east). PW = P-wave velocities (m/s), MS = magnetic susceptibility (10-5 SI). M_z = Mean grain size (Φ), σ_I = sorting (Φ), Sk_I = skewness (Φ), K_G = kurtosis (Φ), all after Folk and Ward (1957). XRF results for Al, Si, Ca, Ti, Fe, Sr, and the log(Ca/Fe), log(Ca/Ti), and log(Si/Ca) ratios.

core 11-01, the sediments gradually change upwards from homogenous very coarse silt to fine sand that is occasionally laminated (mean: 4.8 Φ, sorting: 1.8 Φ). The basal contacts to the sediments below are gradual. The grain size is distributed between 1.3–6.0 % gravel, 9.5–80.7 % sand, 15.4–89.2 % silt, and 0.0–3.6 % clay.

- Between 2.95 and 3.76 mbsf in core 07-03, 1.04 and 1.63 mbsf in core 10-01, 1.00 and 1.50 mbsf in core 10-02, and 2.04 and 3.19 mbsf in core 11-01, the sediments are characterized by bioclastic upwards-coarsening very coarse silt to fine sand and heavy bioturbation (mean: 5.4 Φ, sorting: 1.4 Φ). The basal contacts are sharp in cores 10–01, 10–02, and 11–01 and erosional in the case of core 07-03. The grain size is distributed between 1.1–2.5 % gravel, 9.0–15.9 % sand, 80.1–89.8 % silt, and 0.0–8.3 % clay.
- Between 3.76 and 4.86 mbsf in core 07-03, 1.63 and 3.62 mbsf in core 10-01, 1.50 and 2.40 mbsf in core 10-02, and 3.19 and 4.06 mbsf in core 11-01, all cores are composed of a homogenous fine to medium bioclastic sand (mean: 2.7 Φ, sorting: 0.8 Φ). The grain size is distributed between 0.1–11.8 % gravel, 68.2–98.2 % sand, 1.3–25.1 % silt, and 0.3–5.2 % clay.

Cores 06-01, 12-01, 12-02: cores 06-01, 12-01, and 12-02 recovered 0.75 m, 4.37 m, and 4.34 m of sediment, respectively (Fig. 3A, Table 1).

- Between 0 and 0.31 mbsf in cores 12-01 and 12-02, the top parts comprise normally graded coarse silt or very fine sand. These sediments contain varying amounts of bioclasts and also fully preserved gastropods. In addition, the top parts of both cores have occasional dark organic-rich laminae.
- Between 0 and 0.23 mbsf in core 06-01, 0.31 and 0.40 in cores 12-01 and 12-02, coarser-grained sediments are intercalated. These sediments in core 06-01 consist of fine to medium sand (mean: 2.1 Φ, sorting: 1.4 Φ) with numerous broken shells and an erosional basal surface. The grain size is distributed between 0.0 % gravel, 68.0–100.0 % sand, 0.0–32.0 % silt, and 0.0 % clay. In cores 12-01 and 12-02, these sediments consist of fine sand full of broken shells.
- Between 0.23 and 0.75 mbsf in core 06-01, 0.40 and 1.26 in cores 12-01 and 12-02, the cores comprise normally graded very coarse silt or very fine sand (mean: 3.5 Φ, sorting: 1.7 Φ). The grain size is distributed between 0.0 % gravel, 42.4–80.9 % sand, 19.1–57.6 % silt, and 0.0 % clay. In addition, these sediments contain varying amounts of bioclasts, fully preserved gastropods, and thin shell layers in cores 12-01 and 12-02.
- Between 1.26 and 1.58 mbsf in cores 12-01 and 12-02, the cores consist of heavily bioturbated upwards-coarsening bioclastic medium to coarse sand. Further down-section, between 1.58 and 2.95 mbsf bioclastic very fine sand that is heavily bioturbated follows.
- Between 2.95 and 4.37 mbsf in core 12-01 and 2.95 and 4.34 mbsf in core 12-02, the cores recovered fining-upwards coarse sand with frequent bioclasts and bioturbation at their bases.

Cores 13-01, 13-02: cores 13-01 and 13-02 recovered 4.76 m and 5.27 m of sediment, respectively (Fig. 3A, Table 1).

- Between 0 and 0.22 mbsf, both cores are composed of fining-upwards very coarse silt.
- Between 0.22 and 0.25 mbsf, slightly coarser-grained sediments are intercalated. This deposit has an erosional basal surface and consists of medium sand that fines upwards and is rich in broken bioclasts.
- Between 0.25 and 4.76 mbsf in core 13-01 and 0.25 and 5.27 mbsf in core 13-02, the cores consist of homogeneous fine sand that fines upward into very coarse silt. Occasionally, the fining-upwards sequence is interrupted by finer-grained, coarser-grained, or shell layers and laminae.

4.2.1.1. P-wave velocities, magnetic susceptibility, and XRF results. P-wave velocities, magnetic susceptibility, and XRF results are presented here with the example of core 09-01 (Fig. 4).

- Between 0 and 0.35 mbsf, P-wave velocities are low, and magnetic susceptibility values reach the highest values of the core (mean value of 30×10^{-5} SI). Geochemically, Si, Ca, and Sr values are low, and Ti and Fe values are high.
- Between 0.35 and 0.50 mbsf, P-wave velocities are low in the upper part (0.35–0.45 mbsf) of the coarser-grained deposit. Magnetic susceptibility values are higher than in the surrounding sediments (around 28×10^{-5} SI). Ti and Fe increase, whereas Si, Ca, and Sr slightly decrease compared to the surrounding sediments. The lower part of the coarser-grained deposit (0.45–0.50 mbsf) is characterized by an increase in P-wave velocities up to 2621 m/s, the highest of the whole core. Magnetic susceptibility values are lower than in the surrounding sediments (around 9×10^{-5} SI). Ca and Si increase, Sr increases slightly, and Ti and Fe decrease compared to the surrounding sediments.
- Between 0.50 and 0.98 mbsf, P-wave velocities are still low compared to the lower units. Magnetic susceptibility values are uniform around 14×10^{-5} SI. Si and Ca values are low, and Sr, Ti, and Fe values are high.
- Between 0.98 and 1.43 mbsf, P-wave velocities are highly variable, whereas magnetic susceptibility is uniform. The analyzed elements remain relatively similar to the sediments above.
- Between 1.43 and 2.64 mbsf, the lowermost part of the core is characterized by P-wave velocities between 2000 and 2100 m/s and relatively uniform magnetic susceptibility values between 13 and 16 × 10^{-5} SI. Si, Ca, and Sr values are high, and Fe and Ti are low.

4.2.1.2. Radiocarbon dating. Six shell samples from core 09-01 and, in each case, four shell samples from cores 10-02 and 12-01 were radiocarbon dated (Table 2). They roughly cover the last 11,500 years for core 09-01, the last 9000 years for core 10-02 and the last 10,500 years for core 12-01. The uppermost sample in core 09-01 yielded a comparably old age of 731–1240 cal yr BP (mean: 984 cal yr BP, unmodeled; Table 2).

4.2.2. The western transect

The cores of the western transect can be grouped into group a) cores 19-01, 19-02, 20-01, and 21-01 from an upper plateau, and group b) cores 22-01, 22-02, and 23-01 from a gentle slope towards a lower plateau (Fig. 3B). Stratigraphic and sedimentological characteristics are well preserved in cores 19-01, 19-02, and 19-03.

Cores 19-01, 19-02, 19-03: cores 19-01, 19-02, and 19-03 recovered 3.56 m, 3.65 m, and 3.60 m of sediment, respectively (Fig. 3B, Table 1).

- Between 0 and 1.18 mbsf in core 19-01, 0 and 1.14 mbsf in core 19-02, and 0 and 1.15 mbsf in core 19-03, the uppermost part of the cores consist of very coarse silt to very fine sand that fines upwards (mean: 4.6–3.6 Φ, sorting: 2.7 Φ; Fig. 5). The grain size is distributed between 0.0–7.8 % gravel, 30.4–69.4 % sand, 26.2–60.6 % silt, and 2.3–10.0 % clay.
- Several thin, slightly coarser layers are interbedded in the upper finer-grained sediments of the cores. Most of these slightly coarser layers are shell-rich, show diffuse upper and lower contacts, and are bioturbated.
- Between 0.12–0.14 mbsf, 0.21–0.24 mbsf, 0.35–0.38 mbsf, 0.91–0.93 mbsf in core 19-01, the sediments are slightly coarser than their surroundings (mean grain size: 4.2, 4.1, 3.5, 3.0 Φ, sorting: 2.8, 2.8, 2.8, 2.4 Φ, respectively; Fig. 5). Between 0.12 and 0.14 mbsf, the grain size is distributed between 1.9–3.4 % gravel, 47.7–49.8 % sand, 42.3–43.1 % silt, and 5.8–6.0 % clay. Between 0.21 and 0.24 mbsf, the grain size is distributed between 1.7–3.5 % gravel, 47.7–56.1 % sand, 35.2–43.4 % silt, and 5.2–5.6 % clay. Between 0.21 and 0.24 mbsf, the basal and upper contacts are sharp. Between 0.35 and 0.38 mbsf, the grain size is distributed between 3.2–5.3 % gravel, 55.4–61.0 % sand, 31.7–35.5 % silt, and 3.8–4.3 % clay. Between 0.91 and 0.93 mbsf, the grain size is distributed between 1.3–5.2 % gravel, 59.4–69.4 % sand, 26.8–32.8 % silt, and 2.3–4.7 % clay.

Table 2

Cores 09-01, 10-02, 12-01, 19-01, 19-02, and 22-01 were radiocarbon dated. A total of 33 samples were sent to Beta Analytic Inc. (Florida, USA) and Keck Carbon Cycle AMS Facility (UC Irvine, USA); see Appendix C, Table 1 for further information. Calibration software CALIB 8.2 (Stuiver and Reimer, 1993; Stuiver et al., 2023) with Marine20 (Heaton et al., 2020) and IntCal20 (Reimer et al., 2020) in the case of sample lab code 259343 were used to report the unmodeled cal ^{14}C ages. For sample lab code 259337 CALIBomb (Reimer et al., 2004; Reimer and Reimer, 2023) with NHZ2 (Hua et al., 2013) and IntCal20 (Reimer et al., 2020) was used. In addition, age-specific corrections for local reservoir effects (ΔR) were applied. Modeled cal ^{14}C ages were calculated using an OxCal depositional model (Bronk Ramsey, 2008; Bronk Ramsey and Lee, 2013). Samples from inside the event deposits were excluded from the age-depth model because they are assumed to be older material reworked by the event. See Appendix C for additional information on radiocarbon dating, for further information on local reservoir effects and the creation of the used age-depth models.

Lab code	Sample depth [mbsf]	Material	^{14}C age [yr BP]	ΔR [^{14}C yr]	Unmodeled cal ^{14}C age 2σ, mean age [cal yr BP]	Modeled cal ^{14}C age 2σ, mean age [cal yr BP]
GeoB23509-01 (East)						
236158	0.22	Bivalve (marine)	1485 ± 15	−108 ± 106	731–1240 984	732–1241 983
236159	0.64	Bivalve (marine)	5350 ± 15	407 ± 165	4606–5466 5047	4610–5470 5049
236160	1.00	Bivalve (marine)	6360 ± 15	301 ± 201	5821–6757 6289	5839–6769 6289
236161	1.55	Bivalve (marine)	9515 ± 20	−46 ± 206	9621–10,865 10,265	9952–11,089 10,504
236162	1.94	Bivalve (marine)	10,370 ± 20	−46 ± 206	10,805–12,110 11,476	10,656–11,441 11,049
236163	2.44	Bivalve (marine)	10,385 ± 20	−46 ± 206	10,846–12,153 11,497	11,094–12,267 11,666
GeoB23510-02 (East)						
259337	0.24	Bivalve (marine)	520 ± 20	−49 ± 121	0–56	−2–285 101
259338	0.34	Bivalve (marine)	765 ± 20	−49 ± 121	6–481 271	Not modeled, sample part of Ex
259339	0.76	Bivalve (marine)	6095 ± 15	301 ± 201	5548–6448 6003	5590–6452 6029
259340	1.40	Bivalve (marine)	8245 ± 20	−286 ± 158	8518–9383 8946	8468–9355 8904
GeoB23512-01 (East)						
259333	0.31	Bivalve (marine)	735 ± 20	−49 ± 121	0–455 243	−2–460 248
259334	1.10	Bivalve (marine)	4225 ± 20	50 ± 152	3631–4493 4063	3830–4780 4257
259335	1.63	Gastropod (marine)	8990 ± 20	740 ± 225	8051–9181 8610	7926–9069 8467
259336	2.50	Gastropod (marine)	9740 ± 25	−46 ± 206	10,020–11,173 10,582	9982–11,140 10,534
GeoB23519-01 (West)						
236164	0.21	Bivalve (marine)	650 ± 15	−49 ± 121	0–398 184	−2–304 148
526115	0.57	Bivalve (marine)	2610 ± 30	65 ± 20	1865–2231 2040	1839–2155 2002
236165	0.93	Bivalve (marine)	3205 ± 15	−36 ± 152	2499–3310 2903	2650–3323 2967
259343	1.18	Wood	3950 ± 20	–	4296–4515 4415	Not modeled, sample part of Ey
259341	1.52	Articulated bivalve	4260 ± 20	50 ± 152	3668–4512 4109	Not modeled, sample part of Ey
236166	1.55	Bivalve (marine)	4245 ± 15	50 ± 152	3654–4512 4087	3951–4557 4259
236167	1.67	Bivalve (marine)	5390 ± 20	407 ± 165	4660–5515 5092	4566–5278 4913
236168	3.20	Bivalve (marine)	9230 ± 20	740 ± 225	10,184–11,449 10,820	9954–10,740 10,350
236169	3.50	Bivalve (marine)	9530 ± 20	−46 ± 206	9642–10,896 10,287	10,686–11,460 11,062
GeoB23519-02 (West)						
512669	0.20	Bivalve (marine)	600 ± 30	−49 ± 121	0–366 159	−2–294 142
512670	0.31	Bivalve (marine)	1570 ± 30	−108 ± 106	800–1305 1068	877–1354 1119
512668	1.16	Bivalve (marine)	4280 ± 30	50 ± 152	3689–4562 4135	Not modeled, sample part of Ey
512667	1.56	Bivalve (marine)	4330 ± 30	50 ± 152	3752–4638 4198	4016–4614 4320
512666	2.47	Bivalve (marine)	7910 ± 30	−365 ± 352	7845–9468 8657	7510–8655 8084
512665	3.53	Bivalve (marine)	10,360 ± 30	−46 ± 206	10,790–12,095 11,462	10,795–11,591 11,192
GeoB23522-01 (West)						

Table 2 (*continued*)

Lab code	Sample depth	Material	^{14}C age	ΔR	Unmodeled cal ^{14}C age 2σ, mean age	Modeled cal ^{14}C age 2σ, mean age
	[mbsf]		[yr BP]	[^{14}C yr]	[cal yr BP]	[cal yr BP]
526116	0.69	Bivalve (marine)	2110 ± 30	−95 ± 124	1310–1945 1631	1369–2024 1699
526117	1.20	Bivalve (marine)	3930 ± 30	50 ± 152	3266–4102 3683	3146–4006 3568
526118	3.03	Bivalve (marine)	7740 ± 30	−324 ± 251	7808–9009 8400	8059–9385 8713
526119	3.28	Bivalve (marine)	9670 ± 30	−46 ± 206	9897–11,100 10,490	9602–10,921 10,279

○ Between 0.22–0.25 mbsf, 0.31–0.35 mbsf, and 0.44–0.54 mbsf in core 19-02, the sediments are slightly coarser than their surroundings.
○ Between 0.13 and 0.18 mbsf in core 19-03, the sediments are slightly coarser than their surroundings. Shell fragments are abundant, especially along the basal contact.

• Between 1.18 and 1.53 mbsf in core 19-01, 1.14 and 1.49 mbsf in core 19-02, and 1.15 and 1.55 mbsf in core 19-03, a thick coarse-grained sediment deposit is intercalated (Fig. 5). This deposit consists of four distinctive sections following an erosional basal surface. Shell fragments and small articulated bivalves (<1 cm) can be found throughout sections II, III, and IV.

○ Upper section IV: between 1.18 and 1.22 mbsf in core 19-01, the core consists of very poorly sorted, slightly normally-graded fine sand (mean: 2.6–3.0 Φ, sorting: 2.3 Φ). The grain size is distributed between 0.0–0.4 % gravel, 67.7–94.2 % sand, 5.5–29.0 % silt, and 0.2–3.3 % clay. In the uppermost part, small pieces of wood were found.
○ Upper intermediate section III: between 1.22 and 1.47 mbsf in core 19-01, the core consists of moderately well sorted massive medium sand (mean: 1.4 Φ, sorting: 0.6 Φ). The grain size is distributed between 0.0–0.6 % gravel, 97.2–100.0 % sand, 0.0–2.7 % silt, and 0.0 % clay.
○ Lower intermediate section II: between 1.47 and 1.52 mbsf in core 19-01, the core consists of inversely graded fine to medium sand (mean: 2.0–1.7 Φ, sorting: 1.3 Φ). The grain size is distributed between 0.0–4.4 % gravel, 86.4–99.9 % sand, 0.0–8.1 % silt, and 0.0–1.1 % clay.
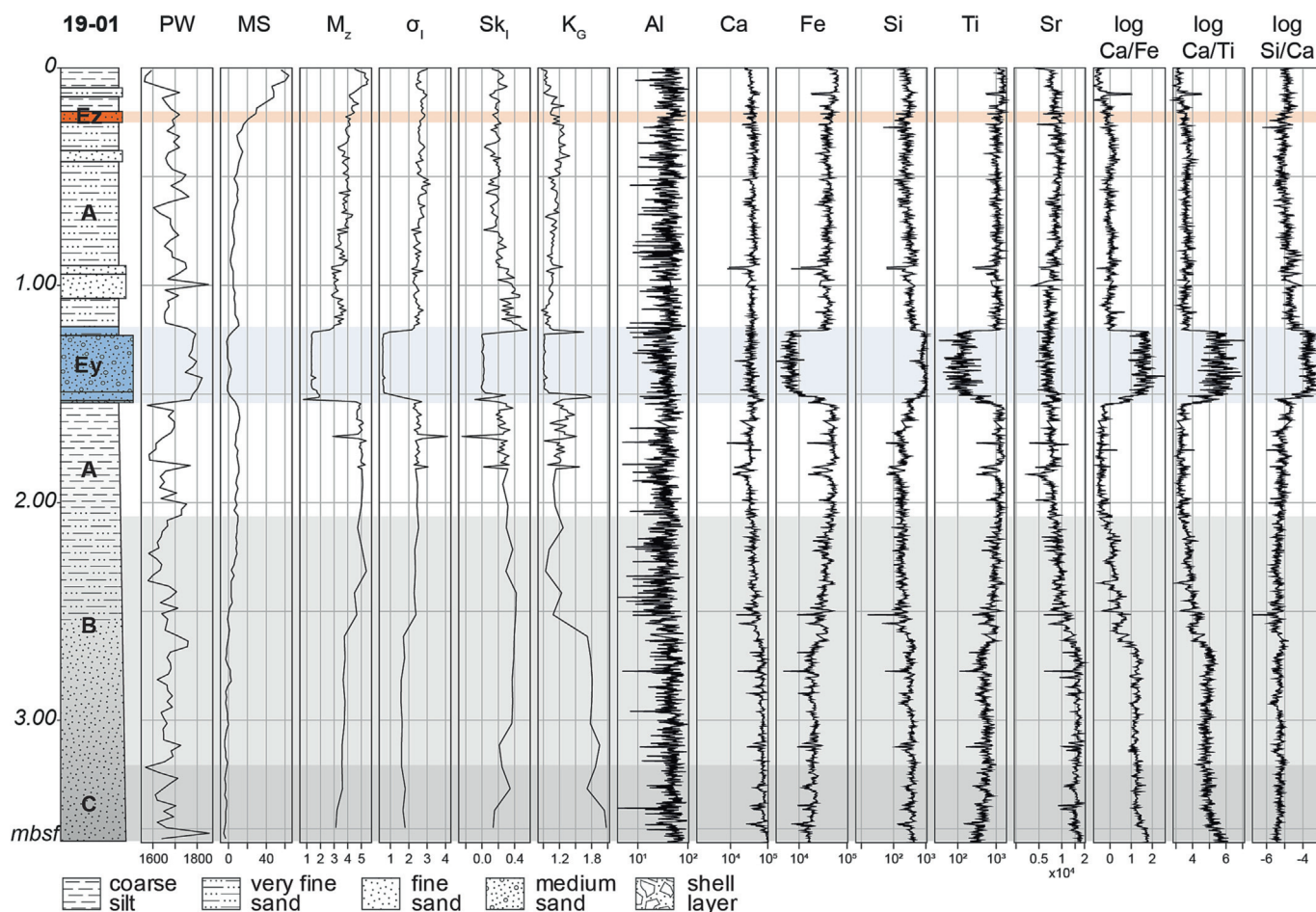

Fig. 5. Structural, textural, compositional properties of 19–01 (West). PW = P-wave velocities (m/s), MS = magnetic susceptibility (10-5 SI). M_z = Mean grain size (Φ), $σ_I$ = sorting (Φ), Sk_I = skewness (Φ), K_G = kurtosis (Φ), all after Folk and Ward (1957). XRF results for Al, Si, Ca, Ti, Fe, Sr, and the log(Ca/Fe), log(Ca/Ti), and log(Si/Ca) ratios.

○ Basal section I: between 1.52 and 1.53 mbsf in core 19-01 is a very poorly sorted coarse shell layer (mean: 0.7 Φ, sorting: 2.2 Φ). The grain size is distributed between 20.7 % gravel, 72.7 % sand, 6.0 % silt, and 0.6 % clay.

- Between 1.53 and approx. 2.40 mbsf in core 19-01, 1.49 and approx. 2.40 mbsf in core 19-02, 1.55 and approx. 2.40 mbsf in core 19-03, the sediments consist of very coarse silt (mean: 4.9 Φ, sorting: 2.5 Φ; Fig. 5). The grain size is distributed between 0.0–17.3 % gravel, 32.1–46.1 % sand, 42.2–58.5 % silt, and 5.4–9.0 % clay. The basal contact with the sediments below is gradual.
- Between approx. 2.40 and the bases of the cores, the basal sediments are composed of poorly sorted, very fine sand that fines upwards (mean: 3.1–3.9 Φ, sorting: 1.7 Φ; Fig. 5). The grain size is distributed between 0.0–3.1 % gravel, 50.2–75.4 % sand, 18.7–42.1 % silt, and 2.3–6.6 % clay.
- At the base of core 19-02 (3.53–3.65 mbsf; Table 1), bedrock consisting of yellowish bioclastic sandstone was retrieved that is bioeroded by boring mollusks (*Pholadidea loscombiana*). Sediments rest unconformably on the bedrock.

Cores 20-01 and 21-01: cores 20-01 and 21-01 are very similar to cores 19-01, 19-02, and 19-03 (Fig. 3B). These cores recovered 3.61 m and 3.14 m of sediment, respectively (Table 1).

- Between 0 and 1.00 mbsf in core 20-01, and 0 and 0.72 mbsf in core 21-01, the uppermost part of the cores consist of very coarse silt that fines upwards (mean: 4.2–5.2 Φ, sorting: 2.0 Φ). The grain size is distributed between 0.0 % gravel, 34.3–54.8 % sand, 38.8–55.2 % silt, and 5.8–10.5 % clay.
- In cores 20-01 and 21-01, slightly coarser layers can be identified between 0.19 and 0.26 mbsf and 0.15 and 0.21 mbsf, respectively (mean: 4.8 Φ, sorting: 2.5 Φ; mean). The grain size is distributed between 0.0 % gravel, 38.6–45.0 % sand, 47.4–52.2 % silt, and 7.6–9.2 % clay. The basal contact is sharp, and the sediment consists of bioclastic fine sand with high amounts of shell debris.
- Between 1.00 and 1.31 mbsf in core 20-01, 0.72 and 0.99 mbsf in core 21-01, a thick deposit is intercalated (mean: 4.3 Φ, sorting: 2.3 Φ). The grain size is distributed between 0.0 % gravel, 36.6–47.1 % sand, 45.8–54.9 % silt, and 6.5–8.7 % clay. This deposit consists of fine sand full of broken shells with a sharp basal contact surface. The upper contact is gradual with upwards-fining grain size.
- Between 1.31 and 2.15 mbsf in core 20-01, 0.99 and 1.95 mbsf in core 21-01, the sediments are composed of very coarse silt that fines upwards (mean: 4.8–5.0 Φ, sorting: 2.0 Φ). The grain size is distributed between 0.0 % gravel, 35.7–48.0 % sand, 45.4–56.1 % silt, and 6.6–8.2 % clay. The basal contacts are gradual.
- Between 2.15 and 3.61 mbsf in core 20-01, 1.95 and 3.14 mbsf in core 21-01, the basal sediments are poorly sorted very fine sands that gradually fine upwards (mean: 3.2–4.8 Φ, sorting: 2.0 Φ). The grain size is distributed between 0.0 % gravel, 34.5–80.9 % sand, 15.7–57.0 % silt, and 3.4–8.5 % clay.

Cores 22-01, 22-02, and 23-01: cores 22-01, 22-02, and 23-01 are very similar to the cores 13-01 and 13-02 of the eastern transect (Fig. 3). The cores recovered 4.21 m, 4.63 m, and 3.23 m of sediment, respectively (Table 1).

- Between 0 and approx. 2.10 mbsf in cores 22-01, 22-02, and 23-01, the uppermost part of the cores consist of very coarse silt that gradually fines upwards (mean: 4.1–5.0 Φ, sorting: 1.8–2.2 Φ). The grain size is distributed between 0.0–7.5 % gravel, 35.3–59.0 % sand, 36.0–57.4 % silt, and 3.8–7.9 % clay. Laminations occur in the lower parts.
- Between approx. 2.10 mbsf and the bases of the cores, the sediments gradually fine upward from fine sand at their bases to very fine sand (mean: 2.9–4.0 Φ, sorting: 1.0–1.9 Φ). The grain size is distributed between 0.0–11.7 % gravel, 61.9–90.1 % sand, 0.0–34.0 % silt, and

0.9–4.0 % clay. The sediments are heavily bioturbated and occasionally interrupted by shelly laminae.

4.2.2.1. P-wave velocities, magnetic susceptibility, and XRF results. P-wave velocities, magnetic susceptibility, and XRF results are presented here with the example of core 19-01 (Fig. 5).

- Between 0 and 1.18 mbsf, P-wave velocities are generally slightly lower than the mean value of 1671 m/s. Magnetic susceptibility gradually increases upwards and reaches a maximum of 60×10^{-5} SI in the uppermost 0.1 mbsf. Si, Ca, and Sr are low, and Ti and Fe increase upwards and reach high values towards the top of the core.
- Most thin, slightly coarser layers interbedded in the finer-grained upper part of the core yielded small peaks in both magnetic susceptibility and P-wave velocity, but they are not discernible in the XRF results. As an exception, the thin layer between 0.21 and 0.24 mbsf, which shows small peaks in magnetic susceptibility and P-wave velocity compared to the surrounding sediments, is also characterized by high Si, Ti, and Fe values with Ca/Fe and Ca/Ti ratios slightly higher at its base. Another contrasting deposit intercalated in the finer-grained sediments between 0.12 and 0.14 mbsf is only discernible by small peaks in both magnetic susceptibility and P-wave velocity and high Si, Ca, Sr, and related ratios. In contrast, Ti, Fe, and corresponding ratios are low.
- Between 1.18 and 1.53 mbsf, magnetic susceptibility drastically decreases to around 0 SI, whereas P-wave velocities strongly increase to a mean value of 1783 m/s. Besides texture (see above), geochemical properties highlight contrasts in sub-units of this coarse-grained deposit.

○ Upper section IV: between 1.18 and 1.22 mbsf, an upward decrease in Si and low Ca and Sr are observed, and an upwards increase in Ti and Fe.
○ Upper intermediate section III: between 1.22 and 1.47 mbsf, high Si, low Ca, Sr, and very low Ti and Fe are observed.
○ Lower intermediate section II: between 1.47 and 1.52 mbsf, Si increases upwards, with a decrease in all other elemental values.
○ Basal section I: between 1.52 and 1.53 mbsf, the core is characterized by a peak in Ca and Sr.

- Between 1.53 and approx. 2.40 mbsf, P-wave velocities gradually decrease while magnetic susceptibility increases upwards. Si, Ca, and Sr are low, and Ti and Fe increase upwards.
- Between approx. 2.40 and 3.56 mbsf, P-wave velocities vary around the mean value of 1671 m/s, and magnetic susceptibility reaches minimum values between -5 and 4×10^{-5} SI. Si, Ca, and Sr are high, and Ti and Fe are low.

4.2.2.2. Radiocarbon dating. Eight shell samples and one wood sample from core 19-01, six shell samples from core 19-02, and four shell samples from core 22-01 were radiocarbon-dated (Table 2). They roughly cover the last 11,500–10,000 years.

5. Stratigraphic units and possible high-energy events

Based on the results of the multi-proxy approach, at least three stratigraphic units and two event layers can be distinguished that represent different sedimentary environments and depositional conditions. P-wave velocities correlate with grain size in continental shelf environments, with lower velocities in fine sediment and higher velocities in coarser sediment (Hamilton and Bachman, 1982). Magnetic susceptibility indicates the relative abundance and magnetic behavior of (magnetic) minerals in the sediment, i.e., if the minerals are ferromagnetic, ferrimagnetic, antiferromagnetic, paramagnetic, or diamagnetic (Dearing, 1999). Low magnetic susceptibility values suggest the presence of, e.g., quartz, alkali-feldspars, calcite, or organic matter, while high magnetic

susceptibility values indicate the presence of Fe-bearing minerals (Dearing, 1999). Al can be linked to detrital input and fine-grained sediment, while Si is associated with the quartz content and, therefore, primarily to sand-sized particles. High Si also suggests increased terrigenous influence on the total sediment. On the other hand, Ca and Sr are commonly correlated to the bioclastic content and carbonates, whereas Fe and Ti are linked to the fine-grained content (e.g., clay), and weathering of siliciclastic rocks as their relative concentrations depend on terrestrial supply. Finally, the log(Ca/Fe) and log(Ca/Ti) ratios indicate biogenic carbonate versus detrital mud as a terrigenous source, and log (Si/Ca) is a proxy for a siliciclastic versus carbonate source (Rothwell et al., 2006; Chagué-Goff et al., 2017).

Stratigraphic units were correlated among the cores by their grain size and elemental and physical properties (Fig. 3). Further, the radiocarbon ages were used to facilitate correlation among the cores. Based on the radiocarbon dates and stratigraphic information provided by the multi-proxy approach, age-depth models were created, and the possible ages of the boundaries between stratigraphic units were modeled (Fig. 6).

5.1. Unit C

Many of the cores consist of a coarser-grained basal part composed of moderately(-well) sorted fine to coarse sand, indicating higher energetic conditions for deposition, i.e., caused by wave or current action. These sediments are characterized by medium to high P-wave velocities, low magnetic susceptibility, and Fe and Ti values, whereas Si, Ca, and Sr values are high, indicating a marine environment rich in quartz particles and calcium carbonate marine shells. We assign these sediments to the lowermost stratigraphic unit C in our cores (Fig. 3). According to the age-depth models, this unit was deposited between ca. 12,000 and 10,000 cal yr BP (Fig. 6). During this time, sea levels were lower than today but rapidly rising from ca. 40 m to ca. 22 m below present level at rates of 9.0 ± 1.7 mm/yr (Dias et al., 2000; Teixeira et al., 2005; Schneider et al., 2010; Trog et al., 2013, 2015; García-Artola et al., 2018). Altogether, this indicates a more proximal and shallower than present shelf depositional environment. Thus, the lowermost unit C is interpreted as a shallow marine deposit based on its properties and composition.

5.2. Unit B

Unit B sediments are generally finer, with an increased proportion of finer particles than in the sandy and matrix-poor materials of unit C. With the grain size change and mud content increase, carbonate bioclasts, total calcium carbonate, and quartz decrease. This variation is mirrored by higher Fe and Ti and is also reflected in higher magnetic susceptibility values. An increase in fine silt and clay indicates less intense hydrodynamic conditions favoring the settling of suspended particles and less ability of coarser terrigenous materials to reach this region of the shelf. This agrees with a substantial increase in the depth of the depositional environment corresponding to a higher mean sea level. The age-depth models (Fig. 6) indicate that unit B accumulated between ca. 7000 and 8000 cal yr BP, correlating with the pronounced deceleration of post-glacial sea-level rise (García-Artola et al., 2018), with mean sea level just a few meters below the present level. Thus, unit B represents the change between rapidly rising sea levels and a subsequent much slower rise, together with the deepening of the depositional environment, making the transition between the former higher-energy sandy lower shoreface and lower-energy muddy shelf environments. In core 09-01, the reflector at around 1 mbsf in the sub-bottom profiles (see chapter 3.1.1) indicates the contact between unit B and uppermost unit A.

5.3. Unit A

The uppermost sediments in the cores are composed of (very) poorly sorted fine sediments. A finer grain size, low amounts of both

bioclasts and carbonate, and higher amounts of mud, in line with high values of Fe, Ti, and magnetic susceptibility, characterize this uppermost unit A. Fe and Ti increase towards the top of the unit, whereas mean grain size, Ca and Si decrease. These properties of unit A, especially the topmost part, indicate calm depositional conditions, which are underlined by the occasional preservation of laminations and an intact Pectinidae in core 09-01. This unit represents the permanent sedimentation regime in a relatively stable marine environment of the mid and outer shelf; thus, it means an adequate archive for event deposits (Weiss and Bahlburg, 2006). Unit A accumulated throughout the last ca. 6000 cal yr BP (Fig. 6). This unit correlates with the stabilization of sea level during the mid to late Holocene (García-Artola et al., 2018) and the subsequent development of coastal barriers and lagoons (Dias et al., 2000; Freitas et al., 2003; Andrade et al., 2016; Costa et al., 2016) along the shore. The sea level was comparable to today (Teixeira et al., 2005; Schneider et al., 2010; Trog et al., 2013, 2015; García-Artola et al., 2018), implying that sediments of unit A were deposited below the mean level of storm-wave base (Hernández-Molina et al., 2000).

5.4. Event deposits

Sedimentary events are typically defined by short and rapid depositional intervals, which strongly contrast with homogeneous background sedimentation (Einsele et al., 1996). In this study, we found that sediments forming unit A, which accumulated under stable background low-energy conditions, contain several intercalations of coarser-grained layers. The coarser layers indicate temporary interruptions of the permanent sedimentation regime of the mid to outer shelf and are interpreted as possible event deposits based on their contrasting textural, geochemical, and lithological characteristics. Two event deposits could be correlated among the cores based on their sedimentological and geochemical signatures and are hereafter referred to as Ey and Ez. Ez is the last remarkable and youngest event layer, and we use the reverse alphabetic letters to express their relative ages. Rapid deposition of the event sediments was assumed to create the age-depth models (Fig. 6). Further, radiocarbon samples taken inside an event layer are considered reworked and thus were excluded from the models.

5.4.1. Event deposit Ez – the 1755 CE tsunami

Ez covers a wide area on the shelf and can be traced in many cores of both transects. It seems to be ubiquitous in the shallower cores of the western transect (cores 19-01: 0.21–0.24 mbsf, 19-02: 0.22–0.25 mbsf, 19-03: 0.13–0.18 mbsf, 20-01: 0.19–0.26 mbsf, 21-01: 0.15–0.21 mbsf) and many cores of the eastern transect (cores 06-01: 0–0.23 mbsf, 07-03: 0.06–0.26 mbsf, 10-01: 0.08–0.48 mbsf, 10-02: 0.10–0.36 mbsf, 11-01: 0.5–0.33 mbsf, 12-01: 0.31–0.40 mbsf, 12-02: 0.31–0.40 mbsf, 13-01: 0.22–0.25 mbsf, 13-02: 0.22–0.25 mbsf). Typical characteristics of Ez are the abrupt increase in grain size, contrasting geophysical and geochemical properties, and higher shell concentrations, especially at the base of the deposit and, in some cores, erosive bases (Fig. 7A). Further, Ez can be identified by its geochemical signature in the deeper cores of the western transect (around 0.20–0.25 mbsf). The spatial distribution of thickness in Ez is somewhat irregular, even when nearby coring sites are compared, but a regional fining trend towards the west and south superimposes this variation. In the western transect and the distal cores of the eastern transect, Ez is relatively thin (0.03–0.09 m thickness). In the proximal cores of the eastern transect, Ez is much thicker (0.20–0.40 m thickness) with differentiation into a lower and an upper section in core 10-01 (Fig. 7A).

Two distinctive sections indicate changes in hydrodynamic conditions during the deposition of Ez in core 10-01 (Fig. 7A). The sediments' coarse grain size and poor sorting indicate a sudden depositional event driven by high energy currents with low sorting capacity. First, the abundance of shell debris at the bottom of the deposit reveals an initial
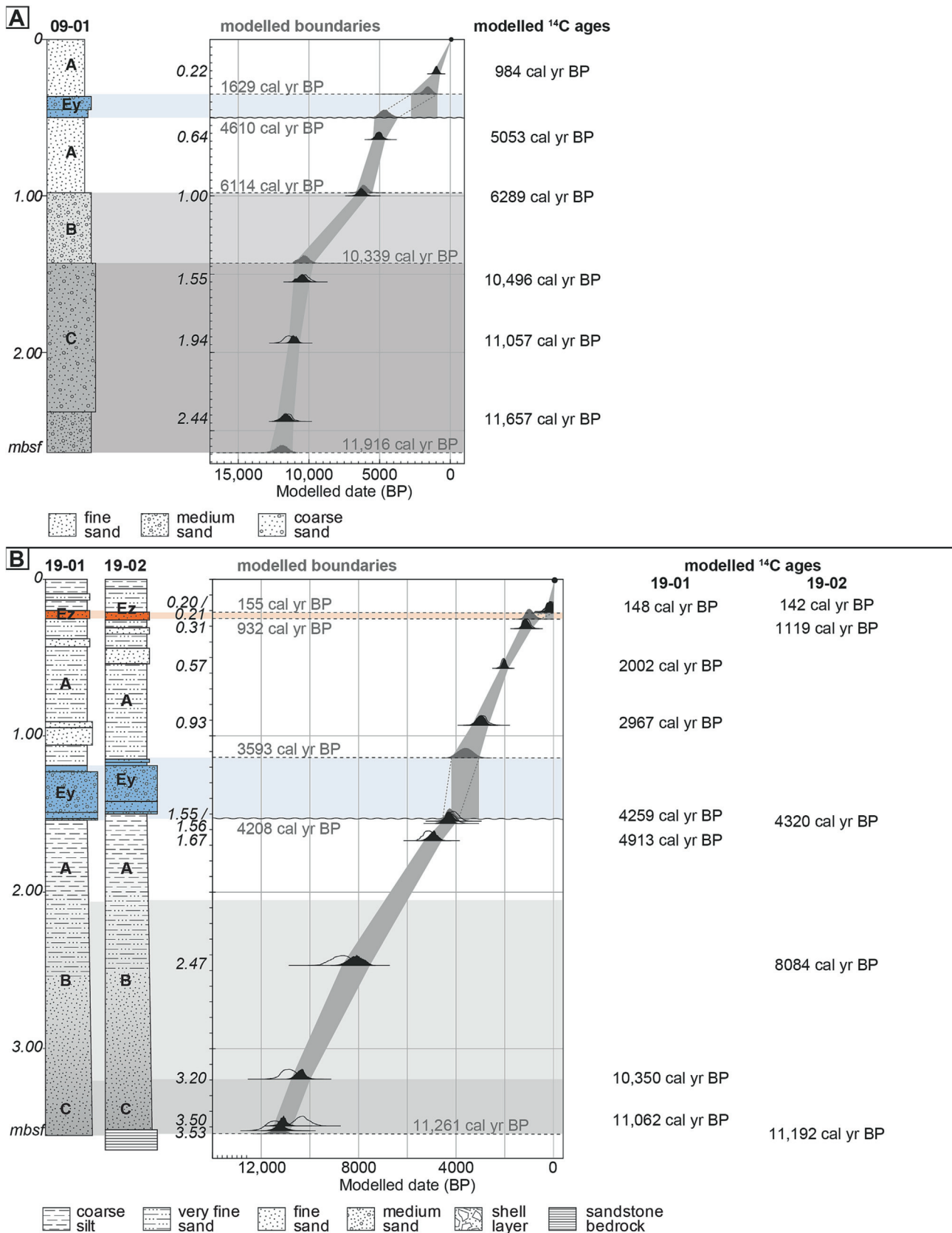
Fig. 6. Age-depth models. A: Age-depth model for core 09-01 based on six radiocarbon ages. The mean modeled boundary ages are marked in grey, and the mean modeled 14C ages for the six radiocarbon samples are marked in black. B: Age-depth model for cores 19-01 and 19-02 based on 12 radiocarbon ages. The mean modeled boundary ages are marked in grey, the mean modeled 14C ages for the seven radiocarbon samples from 19−01, and the five samples from 19−02 are marked in black. Radiocarbon samples taken inside the event deposit Ey are excluded due to reworking.
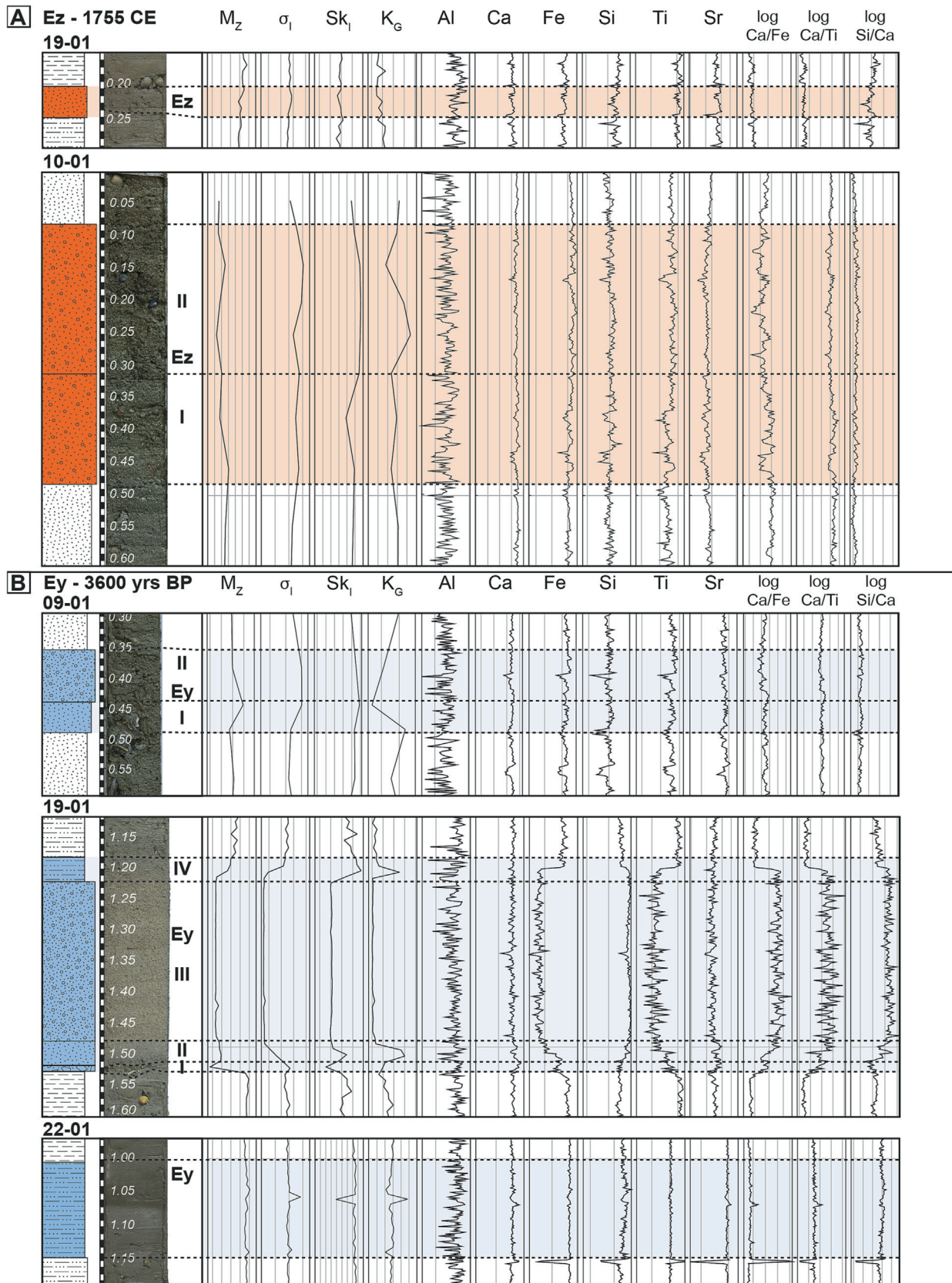
Fig. 7. Event deposits Ex and Ey. A: Photos of event deposit Ex in cores 10-01 and 19-01 with grain size and XRF results B: Photos of event deposit Ey in cores 09-01, 19-01, and 22-01 with grain size and XRF results.

erosion and reworking of the pre-existing shelf bottom materials either by the incoming tsunami wave or the subsequent offshore-directed backwash. Second, the increase in terrigenous components to the top of the event layer points to a later rise in supplies from land or shallower shelf areas. Despite the layer thinning downslope from core 10-01, the imprint of the land-derived sediments can be found in the geophysical and geochemical signatures of the sediment cores. Laterally, the layer also thins, and the sedimentary facies resemble the layer's upper part in core 10-01. Along with the radiocarbon dates and age-depth models (Fig. 6B), Ez can be interpreted as deposits of the 1755 CE Lisbon tsunami.

Abrantes et al. (2008) detected deposits and an erosion gap in cores retrieved from the Tagus River mouth. Based on their high-resolution dating, grain size, XRF-Fe data, and magnetic susceptibility, these imprints were related to the 1755 CE tsunami backwash. In our example, the basal features of the deposit point to a high energy current that eroded and incorporated shelf sediments, while the upper part of the layer is characterized by the introduction of a significant proportion of exotic sediment derived from land or nearshore sources. This upper part can be interpreted as related to tsunami backwash. The sediment-loaded backwash can erode the fine-grained background sediments (incorporating them as dispersed particles or rip-up clasts) and transport coastal to shallow marine deposits (e.g., coarser sand-sized quartz grains; increase in terrestrial geochemical markers) towards the offshore (Feldens et al., 2012; Tamura et al., 2015; Quintela et al., 2016; Riou et al., 2020a, 2020b).

5.4.2. Event deposit Ey – a previously unknown tsunami ca. 3600 cal yr BP

The thicker Ey (Fig. 7B) strongly contrasts with the background sediment in texture and geophysical and geochemical properties (see below) and can be identified in the shallower cores of the western transect (19-01: 1.18–1.53 mbsf, 19-02: 1.14–1.49 mbsf, 19-03: 1.15–1.55 mbsf, 20-01: 1.00–1.31 mbsf, 21-01: 0.72–0.99 mbsf), by its geochemical signature in the deeper cores 22-01 and 22-02 (around 1.00–1.15 mbsf), and possibly in the core from the perched basin of the eastern transect (09-01: 0.35–0.50 mbsf). It also correlates with the strong reflector in the sub-bottom profiles of the western transect. Collective features are an erosional basal surface, a marked increase in grain size, and contrasting geophysical and geochemical properties compared to unit A. A peculiarity of Ey is the complex structure and organization in different sections of the deposit characterized by broad grain-size spectra. However, this structure is strongly variable between cores.

In cores 19-01, 19-02, and 19-03, Ey has a thickness of up to 0.40 m and is organized into four distinctive sections deposited on an erosional basal surface (Fig. 7B). The following shell layer (basal section I) and inversely graded sand (lower intermediate section II) indicate upwards increasing transport capacity (Moore et al., 2011). The massive, visually structureless medium sand (upper intermediate section III) indicates high-energy transport and deposition. Based on the high Si values, high P-wave velocities, and diamagnetic characteristics, quartz-rich sand is the dominant component. On the other hand, Ti and Fe, linked to the mud content, reach their absolute minima. Therefore, a high-energy regime and increased transport capacity are needed to form this thick section III. The normally-graded upper section IV is composed of sediment that settled from the suspension cloud after the high-energy event. Wood fragments found at the top indicate a partially final terrestrial influx. The combined age-depth model for cores 19-01 and 19-02 suggests an age span of 3032–4165 cal yr BP (mean: 3593 cal yr BP, Fig. 6B) for the deposition of Ey. Thus, we refer to this layer as deposited in ca. 3600 cal yr BP in the following. Radiocarbon samples inside the event layer yielded ages similar to the basal contact and are considered reworked material eroded from the seafloor.

This specific deposit configuration (Fig. 7B) is only visible in cores 19-01 and 19-02, the shallowest cores of the western transect just below the steep slope identified in the bathymetry map (Fig. 1). Thus, the hypothesis is introduced that the steeper slope northwest of 19-01

played an essential role in the sediment entrainment, transport and depositional mechanisms related to this specific deposit. The primary sediment source for the quartz-rich medium sand of section III (Fig. 7B) can be found in the proximity of the coring site in shallower water depths (30–35 m), where the present-day bottom sediments are characterized as lithobioclastic medium sand (cf. Instituto Hidrográfico, 2009). We argue that this material was eroded and transported downslope and offshore. The fine-grained matrix of section IV (Fig. 7B) can be interpreted as eroded background material, the secondary sediment source. Larger grains incorporated in the matrix are considered eroded and transported from shallower water depths and the previously deposited section III.

In the western transect, Ey can be traced further downslope to cores 20-01 and 21-01, where it did not imprint a distinct hydroacoustic signal. Grain size tends to become finer, and geophysical and geochemical proxies become less elucidative further offshore. Finally, in cores 22-01 and 22-02, the macroscopic visual identification of this event deposit is no longer possible. However, an increase in relative Si concentrations at around 1.00–1.15 mbsf (Fig. 7B), which probably reflects a higher abundance of quartz, suggests a temporary rise in energy attributed to the deposition of Ey. Thus, the processes leading to the deposition of sediments at coring site 19 were attenuated, and the sediment transport competence diminished further downslope and further offshore.

In core 09-01, a deposit possibly related to Ey can be separated into two sections, indicating different hydrodynamic conditions (Fig. 7B). Section I (at the base) rests upon an abrupt contact and is characterized by low magnetic susceptibility and high P-wave velocities associated with a higher amount of gravel-sized shell fragments. The large shell fragments correlate with high amounts of Ca. A thin mud lamina separates the two sections. Section II (the upper section) presents an increased proportion of muddy sediments and higher magnetic susceptibility, Fe and Ti, compatible with increased influence from terrestrial sources. The very poor sediment sorting in this section indicates a low sorting capacity during high-energy transport and deposition and resembles upper section IV in cores 19-01, 19-02, and 19-03. The age model suggests an age between 913 and 2778 cal yr BP (mean: 1715 cal yr BP; Fig. 6A) for the event deposit with an age between 3704 and 5362 cal yr BP (mean: 4558 cal yr BP; Fig. 6A) for the sediments just below the deposit. However, the modeled age of the event may be underestimated because only one radiocarbon sample is available above the event layer. The modeled age of the sediments just below agrees with the event deposit in core 09-01 being deposited ca. 3600 cal yr BP.

The restricted extension of Ey on the Algarve shelf to the western region of the study area and possibly core 09-01 in the eastern region indicates that the triggering event has affected the Algarve coast severely and left imprints on the continental shelf, at least on a regional scale. In particular, the high-energy characteristics, complex internal structure, and partial terrestrial origin of Ey sediments suggest a driving mechanism related to an offshore-directed flow. However, it remains unclear if the erosive surface at the base of Ey was generated by an onshore-directed current (in such case, providing grounds for the signature of a tsunami) or by the seaward flowing currents (in either case, erosion having preceded the deposition of the event-layer by a brief time interval). Data and discussion above suggest that an extreme event with complex transport mechanisms during backwash deposited layer Ey ca. 3600 cal yr BP. Even though severe storms affect the Portuguese coastlines, a storm wave origin can be excluded for Ey due to a water depth ≥ 65 m, well below the mean level of the storm-wave base. Further, the cores are located in generally calm environments on the shelf. Diagnostic structures like hummocky cross-stratification or wave ripples, which are indicative of storm wave-driven transport and deposition, were not detected in any of our sediment cores. Also, to the best of our knowledge, no corresponding onshore or nearshore tempestites are known in the Algarve region with the same age as Ey. Nevertheless, storm-induced turbidity currents initiated above the storm-wave base flowing offshore

along the seafloor of the shelf and ultimately down the continental slope cannot be excluded as a possible generation mechanism for layer Ey, as well as seismic- or gravity-induced sediment remobilization. However, no indications of turbiditic flow have been found in our cores. Further, seismic- or gravity-induced sediment remobilization is less likely on the flat mid to outer Algarve shelf and would be expected to occur along the continental slope or canyon walls instead (McHugh et al., 2016; Molenaar et al., 2019; Schwestermann et al., 2020).

On the other hand, the erosional basal surfaces (Feldens et al., 2012; Sakuna et al., 2012; Ikehara et al., 2014; Smedile et al., 2020) of the event layers, reworked marine sediments and the input of terrigenous materials that are characteristic for deposit Ey can be linked to offshore tsunami deposits (Feldens et al., 2012; Tamura et al., 2015; Quintela et al., 2016; Riou et al., 2020a, 2020b; Smedile et al., 2020). Similar to Sakuna et al. (2012), we observed different characteristics in sediment sections of Ey that can be attributed to different hydrodynamic conditions that quickly followed each other. These different hydrodynamic conditions are either associated with the inundation and backwash phases or with different pulses of the backwash phase of a tsunami. Furthermore, sediment concentration, grain size, and flow thickness may have played an essential role in the deposit configuration. The lower section(s) of deposit Ey are mainly composed of reworked marine sediments, while the upper section(s) also include terrigenous or coastal materials. The offshore-directed backwash transported large portions of these sediments. Not all of the cores from the southwestern Algarve shelf contain this event's signature, likely because the backwash flow was channeled due to bathymetric features, as observed in other offshore tsunami studies (Abrantes et al., 2008; Dawson and Stewart, 2007; Feldens et al., 2009; Bahlburg and Spiske, 2012; Goodman Tchernov et al., 2016; Riou et al., 2020a, 2020b). Based on the sedimentological properties and accepting the hypothesis of a tsunami origin, Ey is interpreted as related to a tsunami. The other Portuguese offshore tsunami studies (Abrantes et al., 2008; Quintela et al., 2016) did not detect deposits associated with Ey. Abrantes et al. (2008) retrieved cores from the Tagus River mouth near Lisbon, north of our study area. Thus, the event responsible for the deposition of Ey may have affected only the Algarve and adjacent coasts but not reached as far north as Lisbon. Quintela et al. (2016) studied an offshore core retrieved east of our study area (Fig. 1B, C: j). Deposit Ey was only recovered in core 09-01 in the eastern transect, which the channeling of the tsunami backwash or a locally restricted trigger may explain.

5.4.3. Other possible event deposits

In addition to Ey and Ez, thin (centimetric) layers exhibiting sediment coarser than typical unit A materials were found in the cores investigated in this study, particularly in the shallower cores of the western transect. However, a definite identification is problematic due to thinness, a slight contrast to the surrounding sediment, and partly poor preservation of the sediment integrity. In addition, sedimentological and compositional properties can be strongly site-specific. Therefore, only event deposits that can be identified confidently in different depositional areas, i.e., in the western and eastern transects, are used to establish an event record in this study. In this study, only Ez and Ey fulfill this criterion. Possible event deposits that exist only in a single core or location are insufficient to establish the event origin and possible trigger mechanisms. Especially in cores 19-01 and 19-02 of the western transect, several other thin layers of coarser grain size stand out in unit A, which makes the upper parts of the stratigraphy. They only contrast slightly compared to their surroundings and thus cannot be easily identified or traced in other cores due to their thinness, fuzzy boundaries, and poor preservation state, mainly induced by bioturbation. Similar disturbances from soil development have been reported in present-day onshore deposits (Szczuciński, 2012). Therefore, definite statements about the origin of these deposits, their depositional processes, and a correlation among different cores are hardly possible at this point.

Lastly, this study did not detect event deposits correlating with medieval storms and clusters of large floods around 1430–1685 CE and 1730–1810 CE that were identified onshore (Thorndycraft and Benito, 2006). Phases of increased oceanic storminess were inferred by increased coastal sand invasion and dune accretion along the western coast of Portugal during the Little Ice Age (Dias et al., 2000) and the 1770–1830 CE period (Clarke and Rendell, 2016). For comparison, the onshore records of storm events are minimal for the Algarve coast, mainly because large stretches of the coast are eroding. The only known onshore storm deposits are documented in specific locations of Martinhal (Kortekaas and Dawson, 2007) (Fig. 1B, C: a) and the Ria Formosa barrier islands (Andrade et al., 2004) (Fig. 1B: h). No shelf deposits were identified in this study representing marine counterparts of the onshore signatures of increased storminess. These events are expected to have had lower energy than tsunami events that we can find deposits of (i.e., 1755 CE Lisbon tsunami and ca. 3600 cal yr BP tsunami). The cores presented in this study were retrieved below the mean level of the storm-wave base. Thus no storm-wave event signatures are expected, especially at such distances and depths from the coast. However, storm-induced turbidity currents could be expected in these water depths but were not recognized in any of our cores.

6. Discussion

6.1. Tsunamis in the Algarve region – trigger mechanisms

High-energy event deposits like those found intercalated in the fine-grained shelf deposits in cores of the Algarve shelf can derive from different trigger mechanisms, such as floods, storms, and tsunamis, the latter most frequently associated with high-magnitude earthquakes capable of generating rupture of the seafloor, and slope mass movements, both subaerial and submarine. Trigger events, as well as effects, can either be local, regional, or global with varying properties conditioned by local topographic and geological situations (e.g., basement rocks, sediment supply, bathymetry and topography, coastline shape and morphology) or general characteristics (e.g., the behavior of the sediments during transport) (Einsele et al., 1996). Tsunamis in the eastern Central Atlantic, as observed in historical times and inferred from the geological record (Baptista and Miranda, 2009), offer a reasonable and probable source for the rapid changes recorded in sedimentation patterns characterizing those high-energy layers. The sedimentary signatures of the well-known 1755 CE Lisbon tsunami (Ez) and an older event dated to ca. 3600 cal yr BP (Ey) were inferred from significant changes in grain size and other diagnostic features.

The eastern Central Atlantic and Gulf of Cádiz are situated in a seismically active plate-boundary setting (Vázquez et al., 2022). The historical 1755 CE Lisbon earthquake reached a magnitude ≥8 and was felt in the entire Iberian Peninsula and elsewhere along the Atlantic basin. Therefore, a seismic trigger for large tsunamis seems possible, along with other major historical earthquakes. There is also the possibility of submarine mass-wasting capable of generating long-period waves, as suggested by Vázquez et al. (2022), who indicated a landslide-prone area close to the Portimão Bank, around 80 km south of our study area. From the analyses of cores presented in this study, Ey is likely a tsunami deposit correlated in age with a coeval turbidite (or debris flow deposit) discovered at the Marques de Pombal Fault block, southwest of the Algarve shelf (Vizcaino et al., 2006: DF 1). Costa et al. (2022) compiled coastal tsunami deposits in the Portuguese and Gulf of Cádiz coast, and therein Event E5/6 has been documented at several locations. However, the catalog of turbidites caused by potential tsunamigenic earthquakes registered offshore SW Portugal (Gràcia et al., 2010) only includes an isolated coeval event at the Marques de Pombal Fault.

For the onshore record of the Algarve coast, no paleo-tsunami deposits dated to ca. 3600 cal yr BP are known to date. This may be explained by the poor preservation potential of coastal sedimentary archives along the Algarve before ca. 3000 cal yr BP, which is a consequence of their high-energetic setting before the establishment of

coastal barriers, sheltered lagoons, and estuaries (Freitas et al., 2003; Andrade et al., 2016; Costa et al., 2016). However, along the Spanish Gulf of Cádiz coast, paleotsunami deposits of similar age have been found. At the Doñana spit barrier/Guadalquivir marshland, Ruiz et al. (2005) and Lario et al. (2010, 2011) found a tsunami deposit dated to 3900–3700 cal yr BP and Koster and Reicherter (2014) describe a paleotsunami deposit in lowlands of the Barbate-Zahara de los Atunes coast that was dated to ca. 4000 cal yr BP. The dispersion of dates is a significant problem when trying to correlate the diverse event episodes identified along the Spanish coast by different authors (Lario et al., 2010, 2011; Costa et al., 2022). Several factors influence the age calculations and, ultimately, the reported calendar ages, such as the use of different dating techniques, a limited amount of samples analyzed, the use of different substrates or biotic taxa for radiocarbon dating, and the use of the same reservoir effect in different areas regardless of the age and location (Costa et al., 2022). Thus, sedimentary features are wrongly assigned to already known (e.g., documented in historical records) or new events and may explain age discrepancies obtained from sediments deposited by synchronous events. Along the Atlantic coast of Morocco, deposits of comparable but slightly younger age (ca. 3200 cal yr BP) were discovered in the Tahaddart estuary (Khalfaoui et al., 2020). In summary, it seems likely that the ca. 3600 cal yr BP tsunami affected the coastlines of southwestern Iberia and Morocco, at least on a regional scale.

6.2. Offshore tsunami depositional processes

Different local bathymetric conditions (e.g., basins, faults, gentle slopes), varying local sediment sources, and transport paths play an essential role in the offshore deposit configuration (e.g., Feldens et al., 2012). Only a few hundred meters apart, these offshore deposits can present different complexity as well as compositional, geophysical, and geochemical characteristics, like their onshore counterpart. The 1755 CE Lisbon and the ca. 3600 cal yr BP tsunami deposits have substantial differences, even in the same shelf locations, but also similarities. Typical characteristics are erosional basal surfaces, reworked marine sediments, and the input of terrigenous materials, similar to observations in other studies (Sakuna et al., 2012; Feldens et al., 2012; Ikehara et al., 2014; Tamura et al., 2015; Riou et al., 2020a, 2020b; Smedile et al., 2020). Different sections of the deposit attributed to different hydrodynamic conditions (Sakuna et al., 2012) could be identified where deposits are thick enough. Still, the generalization of diagnostic offshore tsunami deposit features is not straightforward and relies on a complex analytical set, including bathymetry and topographic features, geophysical and geochemical proxies, (micro-) paleontology, and sedimentology.

A peculiarity of the ca. 3600 cal yr BP tsunami deposit is the complex structure and organization in up to four different sections that mirror sequential, short-lived, and contrasting hydrodynamic conditions. However, the internal structure and textural, geophysical, and geochemical properties are variable in different cores and locations, and this specific deposit configuration is strongly linked to the local bathymetric conditions. We propose the following transport and deposition conceptual model for the formation of the tsunami deposit in the specific location of core 19 (Fig. 8). First, the seafloor is eroded, and finer grains are lifted in suspension. Part of the suspended materials from the seafloor are transported towards the coast (Fig. 8B). Then, the tsunami backwash induced erosion and flows as an undercurrent along the seafloor, as indicated by bedload transport based on mean grain size. In the first sequence of the backwash, sediments from around 30–35 m water depth are transported downslope in a grain or granular flow (Fig. 8C). Grain-to-grain collision induces dispersive pressure on cohesionless grains to disperse them against gravity (Bagnold, 1956; Lowe, 1976). Traction carpets and inverse grading can be present at the base of these deposits (Lowe, 1976), which is similar to our observations in sections I and II. The following section III consists exclusively of sand-sized particles (97.2–100 % sand); thus, we interpret this part of the ca. 3600 cal yr BP deposit as a grain flow deposit. However, grain flows of medium sand can only form in specific settings at comparably steep slopes (Lowe, 1976), which is why the grain flow deposit is
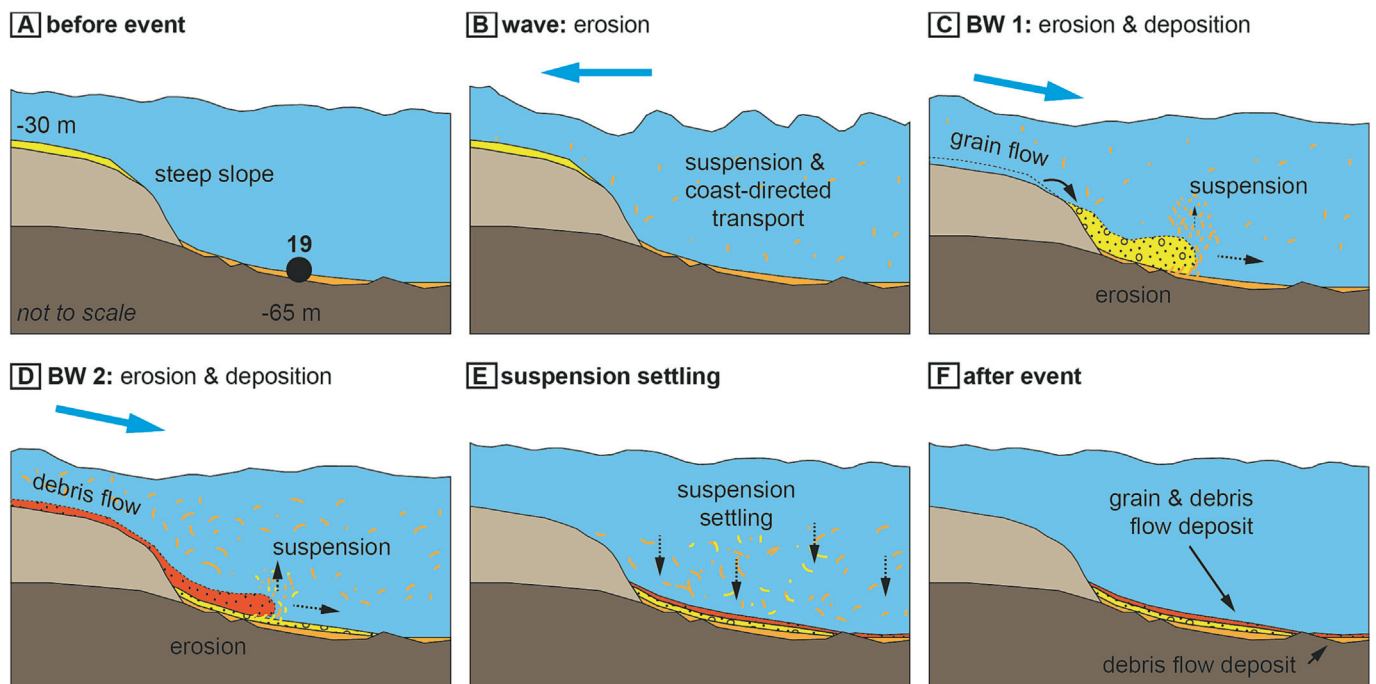
Fig. 8. Generation and deposit structure of the ca. 3600 cal yr BP tsunami deposit (Ey) at coring location 19. A: Coring location 19 is located just at the foot of a relatively steep slope (not to scale). B: Sediment and small shells on the seafloor are eroded and suspended by the onshore-directed flow during the inundation phase of the tsunami. C: Large quantities of medium sand from around 30 m water depth are eroded and transported downslope by the first sequence of the offshore-directed tsunami backwash flow. This first sequence of the tsunami backwash flow resembles a grain flow and deposits the massive medium sand at coring location 19. D: Terrestrial material mixed with marine sediments from the seafloor are transported towards deeper waters by the second sequence of the offshore-directed tsunami backwash flow. This second sequence resembles a debris flow and deposits sand grains and shell fragments in a mud matrix above another erosive surface. E: Fine-grained sediments settle from the water column once the flow has passed. F: The specific deposit configuration with four distinctive sections has only been observed at coring location 19. Further, towards the east and further offshore, the ca. 3600 cal yr BP tsunami deposits only contain debris flow deposits.

restricted to coring site 19 just below a relatively steep slope. When fine-grained particles are also present, a debris flow is produced (Lowe, 1976). True debris flows require a high clay content which was not observed in the cores of this study. However, sandy debris flows as discussed by Hampton (1975), do not require such high clay contents (Shanmugam and Moiola, 1997; Shanmugam, 1997) and are a possible transport and depositional model for section IV at coring site 19 (0.2–3.3 % mud). Also, this is the case of the ca. 3600 cal yr BP tsunami deposits in cores other than 19-01, 19-02, or 19-03. In this second sequence of the backwash, terrigenous materials, coastal sediments, and eroded seafloor particles are moved offshore-directed in a sandy debris flow (Fig. 8D). This sandy debris flow is capable of erosion at its base and topped by fine-grained sediments settling out of the suspension cloud (Fig. 8E). Similar observations were made by Riou et al. (2020a), who describe sediment associated with tsunami backwash that was deposited by a dense and cohesive gravity flow topped by sediments settling out of the suspension cloud.

7. Conclusions

Results presented in this study demonstrate that preservation of tsunami deposits was possible on the Algarve shelf below the storm wave base. However, offshore tsunami research, in general, is limited because accessibility to shelf archives is often complicated (de Martini et al., 2021). Therefore, diagnostic criteria are still very much site-specific, which is also congruent with onshore imprints. Our results suggest that offshore tsunami deposits can only be found at specific locations along the shelf, such as depositional areas in morphological traps or, to a minor extent, in submarine valleys. Observed characteristics can display substantial differences for deposits of the same event. These deposits can contain several marked sections with specific features related to changes in hydrodynamic conditions and sediment supply. The interpretation of paleo-tsunami records of continental shelves faces limitations due to bioturbation and current or wave-induced sediment reworking and transport that characterizes the shelf areas landwards and shallower of the wave base. The latter can be mitigated by choosing to analyze the sedimentary record of generally calm shelf environments (i.e., the deeper parts of the shelf), which are not affected by wave action even under storm conditions. However, bioturbation can severely disturb the sediment structure, especially in thin offshore sediment layers or laminae, as illustrated by the results presented in this study.

On the other hand, our study identified event layers that correlate with the 1755 CE Lisbon tsunami and an older, previously unknown, ca. 3600 cal yr BP tsunami event. Thin deposits do not allow insights into hydrodynamic conditions, but different sections can be separated where the deposits are thick enough. Our findings have extended the tsunami catalogs of Portugal following the detection of event deposits dated to ca. 3600 cal yr BP, of which no counterpart is known yet in the onshore record along the Algarve coast. Offshore tsunami research thus has great potential to extend the tsunami record of any coastal region, especially when coastal records are incomplete or sparse.

Data availability

All data are available in the main text or the appendices. In addition, general information on RV METEOR cruise M152 is published in the cruise report (Reicherter et al., 2019).

Raw data from RV METEOR cruise M152 are published at PANGAEA (Reicherter, 2020; Reicherter and Wölfl, 2020; Reicherter et al., 2021).

Declaration of competing interest

The authors declare that they have no known competing financial interests or personal relationships that could have appeared to influence the work reported in this paper.

Appendix A

Supplementary data to this article can be found online at https://doi.org/10.1016/j.sedgeo.2023.106369.

Appendix A - List of authors who are part of the M152 shipboard scientific party

Appendix B - Geological map

Appendix C - Additional information on radiocarbon dating and age-depth models

References

Abrantes, F., Alt-Epping, U., Lebreiro, S., Voelker, A., Schneider, R., 2008. Sedimentological record of tsunamis on shallow-shelf areas: the case of the 1969 AD and 1755 AD tsunamis on the Portuguese Shelf off Lisbon. Marine Geology 249, 283–293.

Andrade, C., Freitas, M.C., Moreno, J., Craveiro, S.C., 2004. Stratigraphical evidence of late Holocene barrier breaching and extreme storms in lagoonal sediments of Ria Formosa, Algarve, Portugal. Marine Geology 210, 339–362.

Andrade, C., Freitas, M.C., Oliveira, M.A., Costa, P.J.M., 2016. On the sedimentological and historical evidences of seismic-triggered tsunamis on the algarve coast of Portugal. In: Duarte, J.C., Schellart, W.P. (Eds.), Plate Boundaries and Natural Hazards. American Geophysical Union, pp. 219–238.

Arai, K., Naruse, H., Miura, R., Kawamura, K., Hino, R., Ito, Y., Inazu, D., Yokokawa, M., Izumi, N., Murayama, M., Kasaya, T., 2013. Tsunami-generated turbidity current of the 2011 Tohoku-Oki earthquake. Geology 41, 1195–1198.

Bagnold, R.A., 1956. The flow of cohesionless grains in fluids. Philosophical Transactions of the Royal Society of London. Series A, Mathematical and Physical Sciences 249, 235–297.

Bahlburg, H., Spiske, M., 2012. Sedimentology of tsunami inflow and backflow deposits: key differences revealed in a modern example. Sedimentology 59, 1063–1086.

Baptista, M.A., Miranda, J.M., 2009. Revision of the Portuguese catalog of tsunamis. Natural Hazards and Earth System Sciences 9, 25–42.

Baptista, M.A., Miranda, P.M.A., Miranda, J.M., Mendes Victor, L., 1998. Constrains on the source of the 1755 Lisbon tsunami inferred from numerical modelling of historical data on the source of the 1755 Lisbon tsunami. Journal of Geodynamics 25, 159–174.

Baringer, M.O., Price, J.F., 1997. Mixing and spreading of the Mediterranean outflow. Journal of Physical Oceanography 27, 1654–1677.

Baringer, M.O.N., Price, J.F., 1999. A review of the physical oceanography of the Mediterranean outflow. Marine Geology 155, 63–82.

Blott, S.J., Pye, K., 2001. GRADISTAT: a grain size distribution and statistics package for the analysis of unconsolidated sediments. Earth Surface Processes and Landforms 26, 1237–1248.

Brenchley, P.J., 1989. Storm sedimentation. Geology Today 5, 133–137.

Bronk Ramsey, C., 2008. Deposition models for chronological records. Quaternary Science Reviews 27, 42–60.

Bronk Ramsey, C., 2009. Bayesian analysis of radiocarbon dates. Radiocarbon 51, 337–360.

Bronk Ramsey, C., Lee, S., 2013. Recent and planned developments of the program OxCal. Radiocarbon 55, 720–730.

Chagué-Goff, C., Szczuciński, W., Shinozaki, T., 2017. Applications of geochemistry in tsunami research: a review. Earth Science Reviews 165, 203–244.

Clarke, M.L., Rendell, H.M., 2016. Effects of storminess, sand supply and the North Atlantic Oscillation on sand invasion and coastal dune accretion in western Portugal. Holocene 16, 341–355.

Costa, C.N.L., Rita, M.M., 1992. Wave Climatology of the Portuguese Coast [Clima de agitação marítima na costa portuguesa], Technical Report Rel. PT-OM-03/92. Instituto Hidrográfico, Lisbon (in Portuguese with English abstract).

Costa, P.J.M., Andrade, C., Freitas, M.C., Oliveira, M.A., da Silva, C.M., Omira, R., Taborda, R., Baptista, M.A., Dawson, A.G., 2011. Boulder deposition during major tsunami events. Earth Surface Processes and Landforms 36, 2054–2068.

Costa, P.J.M., Andrade, C., Dawson, A.G., Mahaney, W.C., Freitas, M.C., Paris, R., Taborda, R., 2012a. Microtextural characteristics of quartz grains transported and deposited by tsunamis and storms. Sedimentary Geology 275–276, 55–69.

Costa, P.J.M., Andrade, C., Freitas, M.C., Oliveira, M.A., Lopes, V., Dawson, A.G., Moreno, J., Fatela, F., Jouanneau, J.M., 2012b. A tsunami record in the sedimentary archive of the central Algarve coast, Portugal: characterizing sediment, reconstructing sources and inundation paths. Holocene 22, 899–914.

Costa, P.J.M., Oliveira, M.A., González-Villanueva, R., Andrade, C., Freitas, M.C., 2016. Imprints of the AD 1755 tsunami in Algarve (South Portugal) lowlands and post-impact recovery. In: Santiago-Fandiño, V., Tanaka, H., Spiske, M. (Eds.), Tsunamis and Earthquakes in Coastal Environments. Coastal Research Library. 14. Springer, Cham, pp. 17–30.

Costa, P.J.M., Dawson, S., Ramalho, R.S., Engel, M., Dourado, F., Bosnic, I., Andrade, C., 2021. A review on onshore tsunami deposits along the Atlantic coasts. Earth Science Reviews 212, 103441. https://doi.org/10.1016/j.earscirev.2020.103441.

Costa, P.J.M., Lario, J., Reicherter, K., 2022. Tsunami deposits in Atlantic Iberia: a succinct review. In: Álvarez-Martí-Aguilar, M., Machuca Prieto, F. (Eds.), Historical Earthquakes, Tsunamis and Archaeology in the Iberian Peninsula. Natural Science in Archaeology. Springer, Singapore, pp. 105–126.

Dawson, A.G., Stewart, I., 2007. Tsunami deposits in the geological record. Sedimentary Geology 200, 166–183.

De Martini, P.M., Bruins, H.J., Feist, L., Goodman-Tchernov, B.N., Hadler, H., Lario, J., Mastronuzzi, G., Obrocki, L., Pantosti, D., Paris, R., Reicherter, K., Smedile, A., Vött, A., 2021. The Mediterranean Sea and the Gulf of Cadiz as a natural laboratory for paleotsunami research: recent advancements. Earth Science Reviews 216, 103578. https://doi.org/10.1016/j.earscirev.2021.103578.

Dearing, J., 1999. Environmental Magnetic Susceptibility – Using the Bartington MS2 System. Bartington Instruments Ltd. and GMW Associates, San Carlos, CA.

Dias, J.M.A., Boski, T., Rodrigues, A., Magalhães, F., 2000. Coast line evolution in Portugal since the last Glacial Maximum until present — a synthesis. Marine Geology 170, 177–186.

Einsele, G., Chough, S.K., Shiki, T., 1996. Depositional events and their records—an introduction. Sedimentary Geology 104, 1–9.

EMODnet Bathymetry Consortium, 2020. EMODnet Digital Bathymetry (DTM 2020). EMODnet Bathymetry Consortium https://doi.org/10.12770/bb6a87dd-e579-4036-abe1-e649cea9881a.

Feldens, P., Schwarzer, K., Szczucinski, W., Stattegger, K., Sakuna, D., Somgpongchaiykul, P., 2009. Impact of 2004 tsunami on seafloor morphology and offshore sediments, Pakarang Cape, Thailand. Polish Journal of Environmental Studies 18, 63–68.

Feldens, P., Schwarzer, K., Sakuna, D., Szczuciński, W., Sompongchaiyakul, P., 2012. Sediment distribution on the inner continental shelf off Khao Lak (Thailand) after the 2004 Indian Ocean tsunami. Earth, Planets and Space 64, 875–887.

Folk, R.L., Ward, W.C., 1957. Brazos River bar [Texas]; a study in the significance of grain size parameters. Journal of Sedimentary Research 27, 3–26.

Freitas, M.C., Andrade, C., Rocha, F., Tassinari, C., Munhá, J.M., Cruces, A., Vidinha, J., Silva, C.M., 2003. Lateglacial and Holocene environmental changes in Portuguese coastal lagoons: 1. The sedimentological and geochemical records of the Santo André coastal area (SW Portugal). The Holocene 13, 433–446.

García-Artola, A., Stéphan, P., Cearreta, A., Kopp, R.E., Khan, N.S., Horton, B.P., 2018. Holocene sea-level database from the Atlantic coast of Europe. Quaternary Science Reviews 196, 177–192.

Goff, J.A., Austin, J.A., Goodman-Tchernov, B.N., 2018. Estuarine development and early Holocene transgression across an aeolianite substrate, Caesarea, central Israel. Continental Shelf Research 158, 33–44.

Goodman Tchernov, B., Katz, T., Shaked, Y., Qupty, N., Kanari, M., Niemi, T., Agnon, A., 2016. Offshore evidence for an undocumented tsunami event in the 'low risk' Gulf of Aqaba-Eilat, Northern Red Sea. PLoS One 11, e0145802. https://doi.org/10.1371/JOURNAL.PONE.0145802.

Goodman-Tchernov, B.N., Austin, J.A., 2015. Deterioration of Israel's Caesarea Maritima's ancient harbor linked to repeated tsunami events identified in geophysical mapping of offshore stratigraphy. Journal of Archaeological Science: Reports 3, 444–454.

Gràcia, E., Vizcaino, A., Escutia, C., Asioli, A., Rodés, Á., Pallàs, R., Garcia-Orellana, J., Lebreiro, S., Goldfinger, C., 2010. Holocene earthquake record offshore Portugal (SW Iberia): testing turbidite paleoseismology in a slow-convergence margin. Quaternary Science Reviews 29, 1156–1172.

Hamilton, E.L., Bachman, R.T., 1982. Sound velocity and related properties of marine sediments. The Journal of the Acoustical Society of America 72, 1891–1904.

Hampton, M.A., 1975. Competence of fine-grained debris flows. Journal of Sedimentary Petrology 45, 834–844.

Harley, M., Ciavola, P., Camponella, P., 2014. RISC-KIT: Resilience-Increasing Strategies for Coasts - ToolKIT - WEB-GIS impact-oriented database. http://risckit.cloudapp.net/risckit. (Accessed 9 January 2023).

Heaton, T.J., Köhler, P., Butzin, M., Bard, E., Reimer, R.W., Austin, W.E.N, Bronk Ramsey, C., Grootes, P.M., Hughen, K.A., Kromer, B., Reimer, P.J., Adkins, J., Burke, A., Cook, M.S., Olsen, J., Skinner, L.C., 2020. Marine20—the Marine Radiocarbon Age Calibration Curve (0–55,000 cal BP). Radiocarbon 62, 779–820.

Hernández-Molina, F.J., Fernández-Salas, L.M., Lobo, F., Somoza, L., Díaz-del-Río, V., Alveirinho Dias, J.M., 2000. The infralittoral prograding wedge: a new large-scale progradational sedimentary body in shallow marine environments. Geo-Marine Letters 20, 109–117.

Hua, Q., Barbetti, M., Rakowski, A.Z., 2013. Atmospheric radiocarbon for the period 1950–2010. Radiocarbon 55, 2059–2072.

Ikehara, K., Irino, T., Usami, K., Jenkins, R., Omura, A., Ashi, J., 2014. Possible submarine tsunami deposits on the outer shelf of Sendai Bay, Japan resulting from the 2011 earthquake and tsunami off the Pacific coast of Tohoku. Marine Geology 358, 120–127.

Instituto Hidrográfico, 2009. Carta dos Sedimentos Superficiais da Plataforma Continental – Cabo São Vicente ao Rio Guadiana. edition 2. Surface Sediment Map, Instituto Hidrográfico, Lisbon (in Portuguese).

Kaabouben, F., Brahim, A.I., Toto, E., Baptista, M.A., Miranda, J.M., Soares, P., Luis, J.F., 2008. On the focal mechanism of the 26.05.1975 North Atlantic event contribution from tsunami modeling. Journal of Seismology 12, 575–583.

Khalfaoui, O., Dezileau, L., Degeai, J.P., Snoussi, M., 2020. A late Holocene record of marine high-energy events along the Atlantic coast of Morocco: new evidences from the Tahaddart estuary. Geoenvironmental Disasters 7, 1–14.

Kortekaas, S., Dawson, A.G., 2007. Distinguishing tsunami and storm deposits: an example from Martinhal, SW Portugal. Sedimentary Geology 200, 208–221.

Koster, B., Reicherter, K., 2014. Sedimentological and geophysical properties of a ca. 4000 year old tsunami deposit in southern Spain. Sedimentary Geology 314, 1–16.

Krastel, S., Schmincke, H.U., Jacobs, C.L., Rihm, R., le Bas, T.P., Alibés, B., 2001. Submarine landslides around the Canary Islands. Journal of Geophysical Research: Solid Earth 106, 3977–3997.

Lambeck, K., Rouby, H., Purcell, A., Sun, Y., Sambridge, M., 2014. Sea level and global ice volumes from the last Glacial Maximum to the Holocene. Proceedings of the National Academy of Sciences 111, 15296–15303.

Lario, J., Luque, L., Zazo, C., Goy, J.L., Spencer, C., Cabero, A., Bardají, T., Borja, F., Dabrio, C.J., Civis, J., González-Delgado, J.Á., Borja, C., Alonso-Azcárate, J., 2010. Tsunami vs. storm surge deposits: a review of the sedimentological and geomorphological records of extreme wave events (EWE) during the Holocene in the Gulf of Cadiz, Spain. Zeitschrift für Geomorphologie 54, 301–316.

Lario, J., Zazo, C., Goy, J.L., Silva, P.G., Bardaji, T., Cabero, A., Dabrio, C.J., 2011. Holocene palaeotsunami catalogue of SW Iberia. Quaternary International 242, 196–200.

Lowe, D.R., 1976. Grain flow and grain flow deposits. Journal of Sedimentary Research 46, 188–199.

McHugh, C.M., Kanamatsu, T., Seeber, L., Bopp, R., Cormier, M.-H., Usami, K., 2016. Remobilization of surficial slope sediment triggered by the A.D. 2011 M_W 9 Tohoku-Oki earthquake and tsunami along the Japan Trench. Geology 44, 391–394.

Mendes, I., Lobo, F.J., Hanebuth, T.J.J., López-Quirós, A., Schönfeld, J., Lebreiro, S., Reguera, M.I., Antón, L., Ferreira, Ó., 2020. Temporal variability of flooding events of Guadiana River (Iberian Peninsula) during the middle to late Holocene: imprints in the shallow-marine sediment record. Palaeogeography, Palaeoclimatology, Palaeoecology 556, 109900. https://doi.org/10.1016/J.PALAEO.2020.109900.

Molenaar, A., Moernaut, J., Wiemer, G., Dubois, N., Strasser, M., 2019. Earthquake impact on active margins: tracinig surficial remobilization and seismic strengthening in a slope sedimentary sequence. Geophysical Research Letters 46, 6015–6023.

Moore, A., Goff, J., McAdoo, B.G., Fritz, H.M., Gusman, A., Kalligeris, N., Kalsum, K., Susanto, A., Suteja, D., Synolakis, C.E., 2011. Sedimentary deposits from the 17 July 2006 Western Java Tsunami, Indonesia: use of grain size analyses to assess tsunami flow depth, speed, and traction carpet characteristics. Pure and Applied Geophysics 168, 1951–1961.

Mulder, T., Gonthier, E., Lecroart, P., Hanquiez, V., Marches, E., Voisset, M., 2009. Sediment failures and flows in the Gulf of Cadiz (eastern Atlantic). Marine and Petroleum Geology 26, 660–672.

Omira, R., Baptista, M.A., Miranda, J.M., 2011. Evaluating Tsunami impact on the Gulf of Cadiz Coast (Northeast Atlantic). Pure and Applied Geophysics 168, 1033–1043.

Quintela, M., Costa, P.J.M., Fatela, F., Drago, T., Hoska, N., Andrade, C., Freitas, M.C., 2016. The AD 1755 tsunami deposits onshore and offshore of Algarve (south Portugal): sediment transport interpretations based on the study of Foraminifera assemblages. Quaternary International 408, 123–138.

Reicherter, K., 2020. Master Track of METEOR Cruise M152 in 1 sec Resolution (Zipped, 5.3 MB). PANGAEA https://doi.org/10.1594/PANGAEA.922643.

Reicherter, K., Wölfl, A.-C., 2020. Multibeam Bathymetry Raw Data (Kongsberg EM 122 Entire Dataset) of RV METEOR During Cruise M152. PANGAEA https://doi.org/10.1594/PANGAEA.925128.

Reicherter, K., Vött, A., Feist, L., Costa, P.J.M., Schwarzbauer, J., Schüttrumpf, H., Jens, H., Raeke, A., Huhn-Frehers, K., 2019. Lisbon 1755, Cruise no. M152/1, 02.11. -14.11.2018, Funchal (Portugal) - Hamburg (Germany). METEOR-Berichte, Bonn https://doi.org/10.2312/cr_m152.

Reicherter, K., Feist, L., Wölfl, A.-C., 2021. Multibeam Bathymetry Raw Data (Kongsberg EM710 Entire Dataset) of RV METEOR During Cruise M152. PANGAEA https://doi.org/10.1594/PANGAEA.929752.

Reimer, R.W., Reimer, P.J., 2023. CALIBomb. http://calib.org/CALIBomb/. (Accessed 9 January 2023).

Reimer, P.J., Brown, T.A., Reimer, R.W., 2004. Discussion: reporting and calibration of post-bomb 14C data. Radiocarbon 46, 1299–1304.

Reimer, P.J., Austin, W.E.N., Bard, E., Bayliss, A., Blackwell, P.G., Bronk Ramsey, C., Butzin, M., Cheng, H., Edwards, R.L., Friedrich, M., Grootes, P.M., Guilderson, T.P., Hajdas, I., Heaton, T.J., Hogg, A.G., Hughen, K.A., Kromer, B., Manning, S.W., Muscheler, R., Palmer, J.G., Pearson, C., van der Plicht, J., Reimer, R.W., Richards, D.A., Scott, E.M., Southon, J.R., Turney, C.S.M., Wacker, L., Adolphi, F., Büntgen, U., Capano, M., Fahrni, S.M., Fogtmann-Schulz, A., Friedrich, R., Köhler, P., Kudsk, S., Miyake, F., Olsen, J., Reinig, F., Sakamoto, M., Sookdeo, A., Talamo, S., 2020. The IntCal20 Northern Hemisphere radiocarbon age calibration curve (0–55 cal kBP). Radiocarbon 62, 725–757.

Riou, B., Chaumillon, E., Chagué, C., Sabatier, P., Schneider, J.L., Walsh, J.P., Zawadzki, A., Fierro, D., 2020a. Backwash sediment record of the 2009 South Pacific Tsunami and 1960 Great Chilean Earthquake Tsunami. Scientific Reports 2020 (10), 1–13.

Riou, B., Chaumillon, E., Schneider, J.L., Corrège, T., Chagué, C., 2020b. The sediment-fill of Pago Pago Bay (Tutuila Island, American Samoa): new insights on the sediment record of past tsunamis. Sedimentology 67, 1577–1600.

Rothwell, R.G., Hoogakker, B., Thomson, J., Croudace, I.W., Frenz, M., 2006. Turbidite emplacement on the southern Balearic Abyssal Plain (western Mediterranean Sea) during Marine Isotope Stages 1-3: an application of ITRAX XRF scanning of sediment cores to lithostratigraphic analysis. Geological Society, London, Special Publications 267, 79–98.

Ruiz, F., Rodríguez-Ramírez, A., Cáceres, L.M., Vidal, J.R., Carretero, M.I., Abad, M., Olías, M., Pozo, M., 2005. Evidence of high-energy events in the geological record: mid-holocene evolution of the southwestern Doñana National Park (SW Spain). Palaeogeography, Palaeoclimatology, Palaeoecology 229, 212–229.

Sakuna, D., Szczuciński, W., Feldens, P., Schwarzer, K., Khokiattiwong, S., 2012. Sedimentary deposits left by the 2004 Indian Ocean tsunami on the inner continental shelf offshore of Khao Lak, Andaman Sea (Thailand). Earth, Planets and Space 64, 931–943.

Sakuna-Schwartz, D., Feldens, P., Schwarzer, K., Khokiattiwong, S., Stattegger, K., 2015. Internal structure of event layers preserved on the Andaman Sea continental shelf, Thailand: tsunami vs. storm and flash-flood deposits. Natural Hazards and Earth System Sciences 15, 1181–1199.

Schneider, H., Höfer, D., Trog, C., Busch, S., Schneider, M., Baade, J., Daut, G., Mäusbacher, R., 2010. Holocene estuary development in the Algarve Region (Southern Portugal) – a reconstruction of sedimentological and ecological evolution. Quaternary International 221, 141–158.

Schwestermann, T., Huang, J., Konzett, J., Kioka, A., Wefer, G., Ikehara, K., Moernaut, J., Eglinton, I., Strasser, M., 2020. Multivariate statistical and multiproxy constraints on earthquake-triggered sediment remobilization processes in the Central Japan Trench. Geochemistry, Geophysics, Geosystems 21, e2019GC00861. https://doi.org/10.1029/2019GC008861.

Shanmugam, G., 1997. The Bouma Sequence and the turbidite mind set. Earth-Science Reviews 42, 201–229.

Shanmugam, G., Moiola, R.J., 1997. Reinterpretation of depositional processes in a classic flysch sequence (Pennsylvanian Jackfork Group). Ouachita Mountains, Arkansas and Oklahoma. American Association of Petroleum Geologists Bulletin 79, 672–695.

Smedile, A., de Martini, P.M., Pantosti, D., Bellucci, L., del Carlo, P., Gasperini, L., Pirrotta, C., Polonia, A., Boschi, E., 2011. Possible tsunami signatures from an integrated study in the Augusta Bay offshore (Eastern Sicily—Italy). Marine Geology 281, 1–13.

Smedile, A., Molisso, F., Chagué, C., Iorio, M., de Martini, P.M., Pinzi, S., Collins, P.E.F., Sagnotti, L., Pantosti, D., 2020. New coring study in Augusta Bay expands understanding of offshore tsunami deposits (Eastern Sicily, Italy). Sedimentology 67, 1553–1576.

Spiske, M., Tang, H., Bahlburg, H., 2020. Post-depositional alteration of onshore tsunami deposits – implications for the reconstruction of past events. Earth-Science Reviews 202, 103068. https://doi.org/10.1016/j.earscirev.2019.103068.

Stuiver, M., Reimer, P.J., 1993. Extended 14C data base and revised CALIB 3.0 14C age calibration program. Radiocarbon 35, 215–230.

Stuiver, M., Reimer, P.J., Reimer, R., 2023. CALIB radiocarbon calibration, version 8.2. http://calib.org/calib/. (Accessed 9 January 2023).

Szczuciński, W., 2012. The post-depositional changes of the onshore 2004 tsunami deposits on the Andaman Sea coast of Thailand. Natural Hazards 60, 115–133.

Szczuciński, W., 2020. Post-depositional changes to tsunami deposits and their preservation potential. In: Engel., M., Pilarczyk, J., May, S.M., Brill, D., Garett, E. (Eds.), Geological Record of Tsunamis and Other Extreme Waves. Elsevier, pp. 443–469.

Tamura, T., Sawai, Y., Ikehara, K., Nakashima, R., Hara, J., Kanai, Y., 2015. Shallow-marine deposits associated with the 2011 Tohoku-oki tsunami in Sendai Bay, Japan. Journal of Quaternary Science 30, 293–297.

Teixeira, S.B., Gaspar, P., Rosa, M., 2005. Holocene sea-level index points on the Quarteira coast (Algarve, Portugal). Iberian Holocene Paleoenvironmental Evolution – Proceedings Coastal Hope Conference. Universidade de Lisboa, Lisbon, pp. 125–127.

Thorndycraft, V.R., Benito, G., 2006. The Holocene fluvial chronology of Spain: evidence from a newly compiled radiocarbon database. Quaternary Science Reviews 25, 223–234.

Trog, C., Höfer, D., Frenzel, P., Camacho, S., Schneider, H., Mäusbacher, R., 2013. A multiproxy reconstruction and comparison of Holocene palaeoenvironmental changes in the Alvor and Alcantarilha estuaries (southern Portugal). Revue de Micropaleontologie 56, 131–158.

Trog, C., Hempel, R., Frenzel, P., Mäusbacher, R., 2015. Holocene palaeoenvironmental changes in three lagoons on the Algarve coast of Portugal. Paleobiodiversity and Paleoenvironments 95, 203–221.

van den Bergh, G.D., Boer, W., de Haas, H., van Weering, T.C.E., van Wijhe, R., 2003. Shallow marine tsunami deposits in Teluk Banten (NW Java, Indonesia), generated by the 1883 Krakatau eruption. Marine Geology 197, 13–34.

Vázquez, J.-T., Ercilla, G., Alonso, B., Peláez, J.A., Palomino, D., León, R., Bárcenas, P., Casas, D., Estrada, F., Fernández-Puga, M.C., Galindo-Zaldívar, J., Henares, J., Llorente, M., Sánchez-Guillamón, O., d'Acremont, E., Ammar, A., Chourak, M., Fernández-Salas, L. M., López-González, N., Lafuerza, S., 2022. Triggering mechanisms of tsunamis in the Gulf of Cadiz and the Alboran Sea: an overview. In: Álvarez-Martí-Aguilar, M., Machuca Prieto, F. (Eds.), Historical Earthquakes, Tsunamis and Archaeology in the Iberian Peninsula. Natural Science in Archaeology. Springer, Singapore, pp. 65–104.

Vizcaino, A., Gràcia, E., Pallàs, R., Garcia-Orellana, J., Escutia, C., Casas, D., Willmott, V., Diez, S., Asioli, A., Dañobeitia, J., 2006. Sedimentology, physical properties and age of mass transport deposits associated with the Marquês de Pombal Fault, Southwest Portuguese margin. Norwegian Journal of Geology 86, 177–186.

Weiss, R., Bahlburg, H., 2006. A note on the preservation of offshore tsunami deposits. Journal of Sedimentary Research 76, 1267–1273.

Weltje, G.J., Tjallingii, 2008. Calibration of XRF core scanners for quantitative geochemical logging of sediment cores: theory and application. Earth and Planetary Science Letters 274, 423–438.

Weltje, G.J., Bloemsma, M.R., Tjallingii, R., Heslop, D., Röhl, U., Croudace, I.W., 2015. Prediction of geochemical composition from XRF core scanner data: a new multivariate approach including automatic selection of calibration samples and quantification of uncertainties. In: Coudace, I.W., Rothwell, R. (Eds.), Micro-XRF Studies of Sediment Cores. Developments in Paleoenvironmental Research. Springer, Dordrecht, pp. 507–534.

Wentworth, C.K., 1922. A scale of grade and class terms for clastic sediments. The Journal of Geology 30, 377–392.

Wheatcroft, R.A., Drake, D.E., 2003. Post-depositional alteration and preservation of sedimentary event layers on continental margins, I. The role of episodic sedimentation. Marine Geology 199, 123–137.

Wheatcroft, R.A., Wiberg, P.L., Alexander, C.R., Benthley, S.J., Drake, D.E., Harris, C.K., Ogston, A.S., 2007. Post-depositional alteration and preservation of sedimentary strata. In: Nittrouer, C.A., Austin, J.A., Field, M.E., Kravitz, J.H., Syvitski, J.P.M., Wiberg, P.L. (Eds.), Continental Margin Sedimentation: From Sediment Transport to Sequence Stratigraphy. International Association of Sedimentologists. John Wiley & Sons, pp. 101–155.